# NASA Tech Briefs

## NATIONAL AERONAUTICS AND SPACE ADMINISTRATION

Technology Focus

Electronics/Computers

Software

Materials

Mechanics/Machinery

Manufacturing

Bio-Medical

Physical Sciences

Information Sciences

Books and Reports

# INTRODUCTION

Tech Briefs are short announcements of innovations originating from research and development activities of the National Aeronautics and Space Administration. They emphasize information considered likely to be transferable across industrial, regional, or disciplinary lines and are issued to encourage commercial application.

## Availability of NASA Tech Briefs and TSPs

Requests for individual Tech Briefs or for Technical Support Packages (TSPs) announced herein should be addressed to

**National Technology Transfer Center**
Telephone No. **(800) 678-6882** or via World Wide Web at **http://www.nttc.edu/about/contactus.asp**

Please reference the control numbers appearing at the end of each Tech Brief. Information on NASA's Innovative Partnerships Program (IPP), its documents, and services is also available at the same facility or on the World Wide Web at **http://ipp.nasa.gov**.

Innovative Partnerships Offices are located at NASA field centers to provide technology-transfer access to industrial users. Inquiries can be made by contacting NASA field centers listed below.

# NASA Field Centers and Program Offices

**Ames Research Center**
Lisa L. Lockyer
(650) 604-1754
lisa.l.lockyer@nasa.gov

**Dryden Flight Research Center**
Gregory Poteat
(661) 276-3872
greg.poteat@dfrc.nasa.gov

**Glenn Research Center**
Kathy Needham
(216) 433-2802
kathleen.k.needham@nasa.gov

**Goddard Space Flight Center**
Nona Cheeks
(301) 286-5810
nona.k.cheeks@nasa.gov

**Jet Propulsion Laboratory**
Ken Wolfenbarger
(818) 354-3821
james.k.wolfenbarger@jpl.nasa.gov

**Johnson Space Center**
Michele Brekke
(281) 483-4614
michele.a.brekke@nasa.gov

**Kennedy Space Center**
David R. Makufka
(321) 867-6227
david.r.makufka@nasa.gov

**Langley Research Center**
Martin Waszak
(757) 864-4015
martin.r.waszak@nasa.gov

**Marshall Space Flight Center**
Jim Dowdy
(256) 544-7604
jim.dowdy@msfc.nasa.gov

**Stennis Space Center**
John Bailey
(228) 688-1660
john.w.bailey@nasa.gov

**Carl Ray, Program Executive**
Small Business Innovation
Research (SBIR) & Small
Business Technology
Transfer (STTR) Programs
(202) 358-4652
carl.g.ray@nasa.gov

**Doug Comstock, Director**
Innovative Partnerships
Program Office
(202) 358-2560
doug.comstock@nasa.gov

# Improved Instrument for Detecting Water and Ice in Soil
### This device can be used to assess ice buildup on aircraft.

*NASA's Jet Propulsion Laboratory, Pasadena, California*

An instrument measures electrical properties of relatively dry soils to determine their liquid water and/or ice contents. Designed as a prototype of instruments for measuring the liquid-water and ice contents of lunar and planetary soils, the apparatus could also be utilized for similar purposes in research and agriculture involving terrestrial desert soils and sands, and perhaps for measuring ice buildup on aircraft surfaces.

This instrument is an improved version of the apparatus described in "Measuring Low Concentrations of Liquid Water and Ice in Soil" (NPO-41822), *NASA Tech Briefs*, Vol. 33, No. 2 (February 2009), page 22. The designs of both versions are based on the fact that the electrical behavior of a typical soil sample is well approximated by a network of resistors and capacitors in which resistances decrease and capacitances increase (and the magnitude and phase angle of impedance changes accordingly) with increasing water content. The previous version included an impedance spectrometer and a jar into which a sample of soil was placed. Four stainless-steel screws at the bottom of the jar were used as electrodes of a four-point impedance probe connected to the spectrometer.

The present instrument does not include a sample jar and can be operated without acquiring or handling samples. Its impedance probe consists of a compact assembly of electrodes housed near the tip of a cylinder. The electrodes protrude slightly from the cylinder (see Figure 1). In preparation for measurements, the cylinder is simply pushed into the ground to bring the soil into contact with the electrodes.

A typical measurement run takes several seconds. Typically, the magnitude and phase angle of impedance are measured as function of frequency from 20 Hz to 500 kHz. Figure 2 presents some results of test measurements performed at temperatures from –25 to +65 °C on dry and moist silica sand. From these and other measurement results, it was concluded that, in the aforementioned temperature range, the instrument can detect the presence of water or ice at a concentration as low 0.1 weight percent and can measure the concentration above 0.5 weight percent.

Figure 1. The **Water/Ice Detection Instrument** relies on an electrical properties probe using a two-probe pair. In use, the free end is pushed into the ground to place the electrodes in contact with the soil.
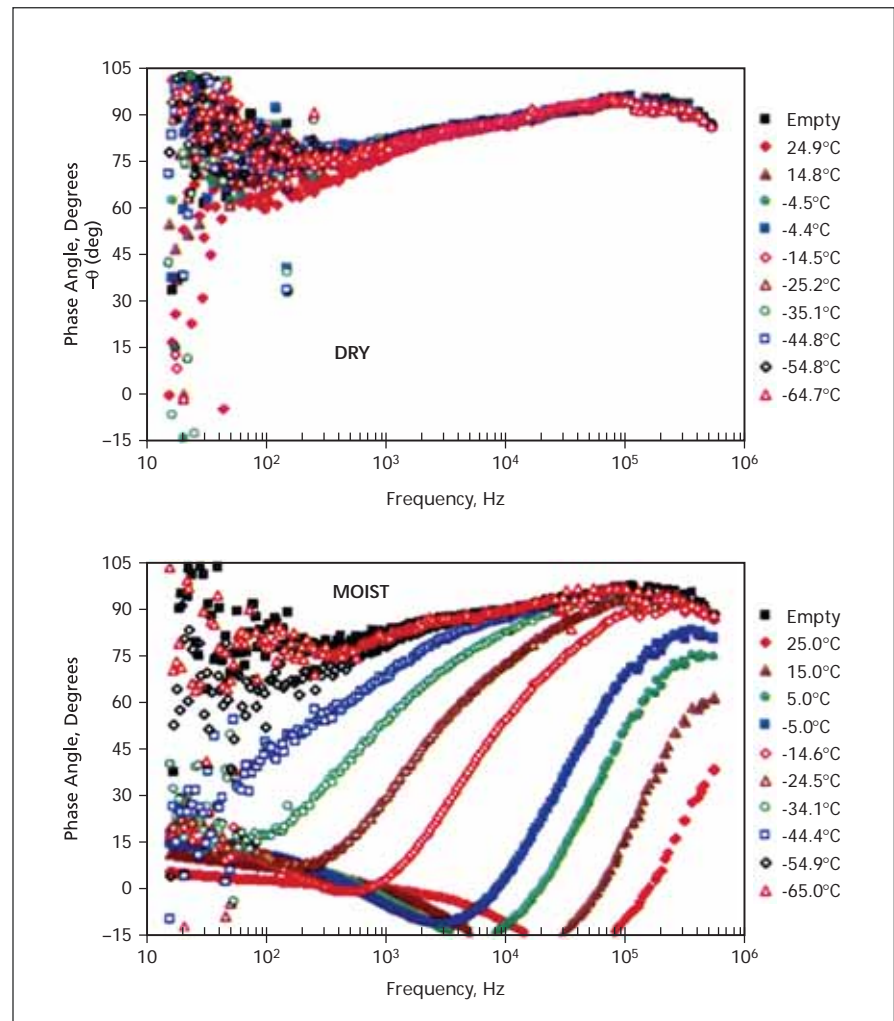


Figure 2. **Phase Angle Versus Frequency** was measured in the "empty" case (nothing in contact with the electrodes) and at various temperatures with electrodes in contact with (a) dry silica sand and (b) silica sand moistened with 0.1 weight percent of a 0.1 M aqueous solution of KCl.

# Real-Time Detection of Dust Devils From Pressure Readings

**Dust devils are identified as large deviations from a sliding polynomial fit.**

*NASA's Jet Propulsion Laboratory, Pasadena, California*

A method for real-time detection of dust devils at a given location is based on identifying the abrupt, temporary decreases in atmospheric pressure that are characteristic of dust devils as they travel through that location. The method was conceived for use in a study of dust devils on the Martian surface, where bandwidth limitations encourage the transmission of only those blocks of data that are most likely to contain information about features of interest, such as dust devils. The method, which is a form of intelligent data compression, could readily be adapted to use for the same purpose in scientific investigation of dust devils on Earth.

In this method, the readings of an atmospheric-pressure sensor are repeatedly digitized, recorded, and processed by an algorithm that looks for extreme deviations from a continually updated model of the current pressure environment. The question in formulating the algorithm is how to model current "normal" observations and what minimum magnitude deviation can be considered sufficiently anomalous as to indicate the presence of a dust devil. There is no single, simple answer to this question: any answer necessarily entails a compromise between false detections and misses.

For the original Mars application, the answer was sought through analysis of sliding time windows of digitized pressure readings. Windows of 5-, 10-, and 15-minute durations were considered. The windows were advanced in increments of 30 seconds. Increments of other sizes can also be used, but computational cost increases as the increment
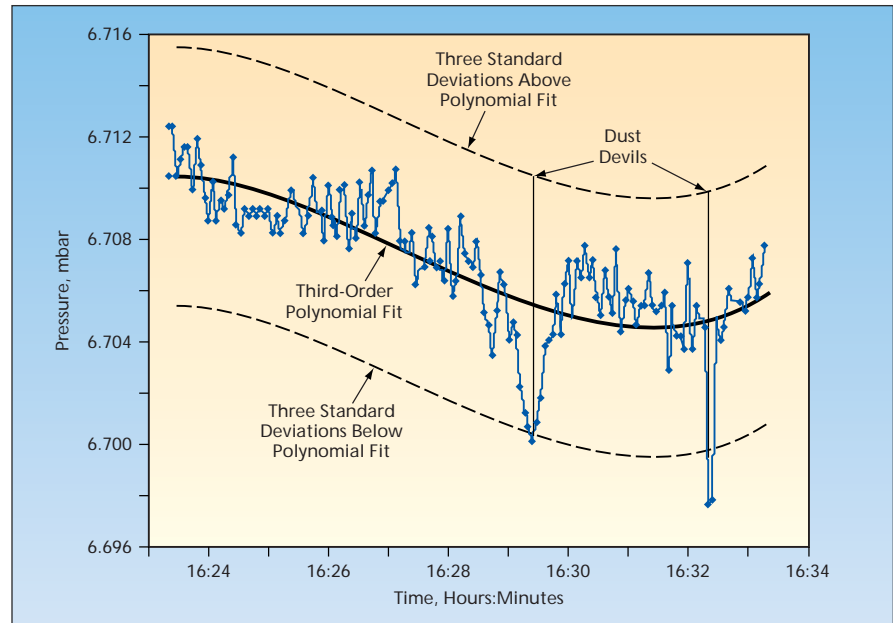


A **Third-Order Polynomial Fit** with 3-standard-deviation limits was superimposed on a 10-minute sliding time window of Mars atmospheric-pressure readings. Two dust devils were detected as negative deviations of more than 3 standard deviations.

decreases and analysis is performed more frequently. Pressure models were defined using a polynomial fit to the data within the windows. For example, the figure depicts pressure readings from a 10-minute window wherein the model was defined by a third-degree polynomial fit to the readings and dust devils were identified as negative deviations larger than both 3 standard deviations (from the mean) and 0.05 mbar in magnitude. An algorithm embodying the detection scheme of this example was found to yield a miss rate of just 8 percent and a false-detection rate of 57

percent when evaluated on historical pressure-sensor data collected by the Mars Pathfinder lander. Since dust devils occur infrequently over the course of a mission, prioritizing observations that contain successful detections could greatly conserve bandwidth allocated to a given mission. This technique can be used on future Mars landers and rovers, such as Mars Phoenix and the Mars Science Laboratory.

*This work was done by Kiri Wagstaff of Caltech for NASA's Jet Propulsion Laboratory. Further information is contained in a TSP (see page 1). NPO-44724*

# Determining Surface Roughness in Urban Areas Using Lidar Data

**An automatic derivation of relevant parameters estimates surface roughness.**

*Stennis Space Center, Mississippi*

An automated procedure has been developed to derive relevant factors, which can increase the ability to produce objective, repeatable methods for determining aerodynamic surface roughness. Aerodynamic surface roughness is used for many applications, like

atmospheric dispersive models and wind-damage models. For this technique, existing lidar data was used that was originally collected for terrain analysis, and demonstrated that surface roughness values can be automatically derived, and then subsequently utilized

in disaster-management and homeland-security models.

The developed lidar-processing algorithm effectively distinguishes buildings from trees and characterizes their size, density, orientation, and spacing (see figure); all of these variables are param-

**Processed Lidar Data** (left) and **Aerial Imagery** (right) show a one-square-kilometer area of Broward County, Florida.

eters that are required to calculate the estimated surface roughness for a specified area. By using this algorithm, aerodynamic surface roughness values in urban areas can then be extracted automatically. The user can also adjust the algorithm for local conditions and lidar characteristics, like summer/winter vegetation and dense/sparse lidar point spacing. Additionally, the user can also survey variations in surface roughness that occurs due to wind direction; for example, during a hurricane, when wind direction can change dramatically, this variable can be extremely significant.

In its current state, the algorithm calculates an estimated surface roughness for a square kilometer area; techniques using the lidar data to calculate the surface roughness for a "point," whereby only roughness elements that are upstream from the point of interest are used and the wind direction is a vital concern, are being investigated. This technological advancement will improve the reliability and accuracy of models that use and incorporate surface roughness.

# ◉ DSN Data Visualization Suite

*NASA's Jet Propulsion Laboratory, Pasadena, California*

The DSN Data Visualization Suite is a set of computer programs and reusable Application Programming Interfaces (APIs) that assist in the visualization and analysis of Deep Space Network (DSN) spacecraft-tracking data, which can include predicted and actual values of downlink frequencies, uplink frequencies, and antenna-pointing angles in various formats that can include tables of values and polynomial coefficients. The data can also include lists of antenna-pointing events, lists of antenna-limit events, and schedules of tracking activities.

To date, analysis and correlation of these intricately related data before and after tracking have been difficult and time-consuming. The DSN Data Visualization Suite enables operators to quickly diagnose tracking-data problems before, during, and after tracking. The Suite provides interpolation on demand and plotting of DSN tracking data, correlation of all data on a given temporal point, and display of data with color coding configurable by users. The suite thereby enables rapid analysis of the data prior to transmission of the data to DSN control centers. At the control centers, the same suite enables operators to validate the data before committing the data to DSN subsystems. This software is also Web-enabled to afford its capabilities to international space agencies.

# Electronics/Computers

# Hamming and Accumulator Codes Concatenated With MPSK or QAM

**Multiple constituent codes would be utilized in a high-speed parallel architecture.**

*NASA's Jet Propulsion Laboratory, Pasadena, California*

In a proposed coding-and-modulation scheme, a high-rate binary data stream would be processed as follows:

1. The input bit stream would be demultiplexed into multiple bit streams.
2. The multiple bit streams would be processed simultaneously into a high-rate outer Hamming code that would comprise multiple short constituent Hamming codes — a distinct constituent Hamming code for each stream.
3. The streams would be interleaved. The interleaver would have a block structure that would facilitate parallelization for high-speed decoding.
4. The interleaved streams would be further processed simultaneously into an inner two-state, rate-1 accumulator code that would comprise multiple constituent accumulator codes — a distinct accumulator code for each stream.
5. The resulting bit streams would be mapped into symbols to be transmitted by use of a higher-order modulation — for example, M-ary phase-shift keying (MPSK) or quadrature amplitude modulation (QAM).

The novelty of the scheme lies in the concatenation of the multiple-constituent Hamming and accumulator codes and the corresponding parallel architectures of the encoder and decoder circuitry (see figure) needed to process the multiple bit streams simultaneously. As in the cases of other parallel-processing schemes, one advantage of this scheme is that the overall data rate could be much greater than the data rate of each encoder and decoder stream and, hence, the encoder and decoder could handle data at an overall rate beyond the capability of the individual encoder and decoder circuits. A less-obvious advantage is that the scheme would utilize bandwidth efficiently and would make it possible to reduce transmitter power by about 2 dB without exceeding a given bit-error rate for the best prior coding-and-modulation scheme.

In one instantiation of the scheme, the outer code would consist of 372 Hamming codes characterized by a block length of 15 symbols, of which 11 would be information symbols [denoted a (15,11) code in the art]. The inner code would consist of 15 rate-1, two-state accumulator codes of block length 372. The parallel nature of the interleaver would enable the permutation of the 15 symbols of each of the 372 Hamming code words by 372



PART OF TRANSMITTER CONTAINING ENCODER

PART OF RECEIVER CONTAINING DECODER
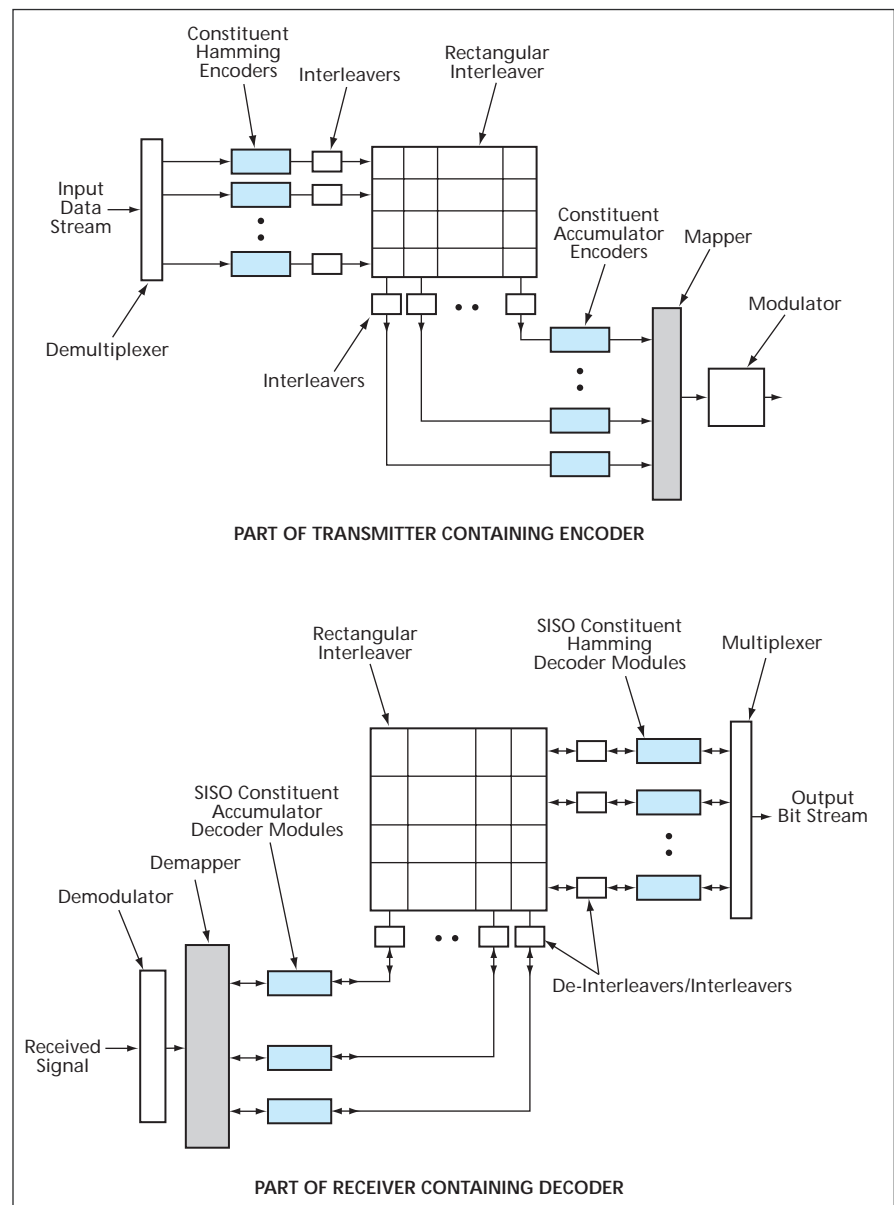
The **Encoder and Decoder** would concatenate and interleave an outer set of parallel constituent Hamming codes with an inner set of parallel constituent accumulator codes.

independent interleavers, and the 15 groups of 372 Hamming symbols would be permuted by 15 independent interleavers before being fed to the 15 accumulators. This code structure at the transmitter would enable the use, in the receiver, of a high-speed iterative decoder that could include 372 soft-input, soft-output (SISO) modules to decode the 372 constituent Hamming codes in parallel and 15 SISO modules to decode the 15 constituent accumulator codes in parallel. Hence, the overall decoder could have a parallel architecture.

# Wide-Angle-Scanning Reflectarray Antennas Actuated by MEMS
## These could be simpler, cheaper alternatives to electronically scanned phased-array antennas.

*NASA's Jet Propulsion Laboratory, Pasadena, California*

An effort to develop large-aperture, wide-angle-scanning reflectarray antennas for microwave radar and communication systems is underway. In an antenna of this type as envisioned, scanning of the radiated or incident microwave beam would be effected through mechanical rotation of the passive (reflective) patch antenna elements, using microelectromechanical systems (MEMS) stepping rotary actuators typified by piezoelectric micromotors. It is anticipated that the cost, mass, and complexity of such an antenna would be less than, and the reliability greater than, those of an electronically scanned phased-array antenna of comparable beam-scanning capability and angular resolution.

In the design and operation of a reflectarray, one seeks to position and orient an array of passive patch elements in a geometric pattern such that, through constructive interference of the reflections from them, they collectively act as an efficient single reflector of radio waves within a desired frequency band. Typically, the patches lie in a common plane and radiation is incident upon them from a feed horn. Certain phase-sensitive types of such elements can be clocked to predetermined angles, relative to those of their neighbors, to modify the phase of the radiation incident from the feed horn and reflected from the elements so as to, for example, make the a flat array of patches act as though it were a parabolic reflector.

Another reflectarray characteristic, essential to the present development, is that if the patch elements are rotated in unison, then the beam radiated by the antenna can be steered in elevation and azimuth through angular displacements of as much as ±50°. In an antenna of the type under development, the patch elements would be phase-sensitive in the sense mentioned above, would be circularly polarized, and would be mounted on the shafts of MEMS stepping rotary actuators (see figure). The maximum range of element rotation needed for wide-angle beam scanning would be only about ±180°, and scanning could be effected by use of relatively coarse rotational steps.



Feed Horn    Patch Antenna Element    MEMS Stepping Rotary Actuator
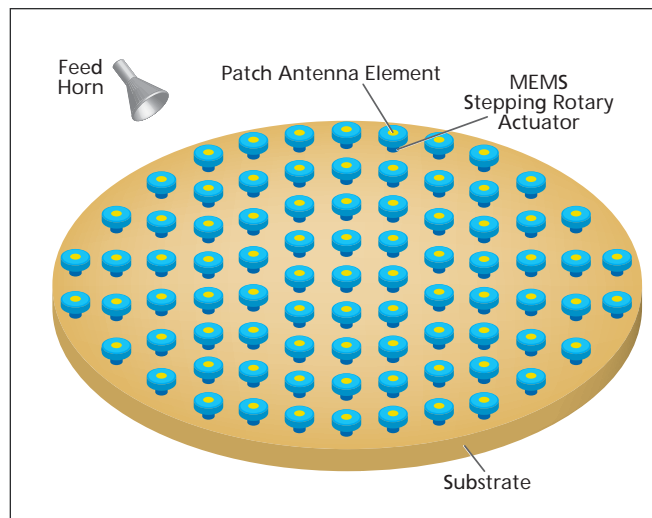
Substrate

**Passive Patch Antenna Elements** in an array would be mounted on shafts of MEMS stepping rotary actuators that, in turn, would be mounted on a common substrate. The patch elements would be circularly polarized, and would be phase-sensitive in the sense that each would alter the phase difference between incident and reflected radiation by an amount that would depend on the actuator shaft angle.

# Biasable Subharmonic Membrane Mixer for 520 to 600 GHz
## This is a prototype of mixers for future submillimeter-wavelength spectrometers.

*NASA's Jet Propulsion Laboratory, Pasadena, California*

The figure shows a biasable subharmonic mixer designed to operate in the frequency range from 520 to 600 GHz. This mixer is a prototype of low-power mixers needed for development of wideband, high-resolution spectrometers for measuring spectra of molecules in the atmospheres of Earth, other planets, and comets in the frequency range of 400 to 700 GHz.

Three considerations dictated the main features of the design:
• It is highly desirable to operate the spectrometers at or slightly below room temperature. This consideration is addressed by choosing Schottky diodes as the frequency-mixing circuit elements because of all mixer diodes, Schottky diodes are the best candidates for affording sufficient sensitivity at or slightly below room-temperature range.
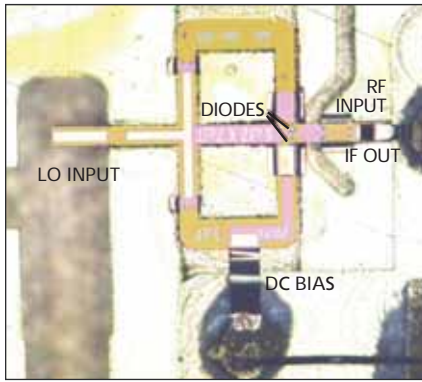
This **Biasable Subharmonic Mixer** for the RF range of 520 to 600 GHz consists of a monolithic integrated circuit on a GaAs membrane held in a precision-machined waveguide block.

- The short wavelengths in the intended operating-frequency range translate to stringent requirements for precision of fabrication and assembly of the circuits; these requirements are even more stringent for wide-bandwidth circuits. This consideration is addressed in two ways: (1) As much as possible of the mixer circuitry is fabricated in the form of a monolithic integrated circuit on a GaAs membrane, employing a modified version of a process used previously to fabricate a non-subharmonic mixer for a frequency of 2.5 THz and frequency multipliers for frequencies up to 2 THz. (2) The remainder of the circuitry is precision machined into a waveguide block that holds the GaAs integrated circuit.

- Generation of a local-oscillator (LO) signal having sufficient power to pump a mixer requires more DC power as the LO frequency increases; this is because the only wide-band LO sources available in this frequency range are Schottky-diode frequency multipliers, and their efficiencies decrease with frequency. This consideration is addressed in two ways: (1) Unlike the prior 2.5-THz GaAs-membrane mixer, this mixer is subharmonically driven, meaning that the LO operates at half the frequency of the incoming signal to be measured [denoted the radio frequency (RF) in traditional frequency mixer parlance]. (2) The diodes are arranged so that they can be biased to operate closer to their switching voltage so that less LO power is needed to switch the diodes between the conducting and nonconducting states. This switching is what makes the diodes act as a frequency mixer.

The Schottky diodes are fabricated in an antiparallel configuration, using beam leads, such that one electrode of each diode is grounded. One diode is AC grounded through a capacitor to allow the diodes to be biased. A simple probe picks up the LO signal from a waveguide shown on the left side of the figure. The LO signal bypasses an RF filter comprised of two vertical stubs and is coupled into the mixer diodes. Similarly, another probe picks up the RF signal from a waveguide shown on the right side of the figure and the RF signal flows leftward to the diodes.

The on-chip circuitry also conveys the lower-frequency mixer output signal [also denoted, variously, as the intermediate-frequency (IF) signal or the down-converted version of the RF signal in traditional frequency-mixer parlance] to an off-chip circuit board on the right side. The stub filter to the left of the diodes prevents the leakage of the RF signal past the diodes to the LO waveguide. Leakage of the LO signal into the RF waveguide is inherently blocked as it is below the cutoff frequency of the RF waveguide. There is also a filter in the output channel, implemented as shunt capacitors (not shown here), to prevent leakage of RF and LO signals to the off-chip circuitry that processes the IF signal.

# Hardware Implementation of Serially Concatenated PPM Decoder

## Error-rate performance approaches channel capacity.

*NASA's Jet Propulsion Laboratory, Pasadena, California*

A prototype decoder for a serially concatenated pulse position modulation (SCPPM) code has been implemented in a field-programmable gate array (FPGA). At the time of this reporting, this is the first known hardware SCPPM decoder. The SCPPM coding scheme, conceived for free-space optical communications with both deep-space and terrestrial applications in mind, is an improvement of several dB over the conventional Reed-Solomon PPM scheme. The design of the FPGA SCPPM decoder is based on a turbo decoding algorithm that requires relatively low computational complexity while delivering error-rate performance within approximately 1 dB of channel capacity.

The SCPPM encoder consists of an outer convolutional encoder, an interleaver, an accumulator, and an inner modulation encoder (more precisely, a mapping of bits to PPM symbols). Each code is describable by a trellis (a finite directed graph). The SCPPM decoder consists of an inner soft-in-soft-out (SISO) module, a de-interleaver, an outer SISO
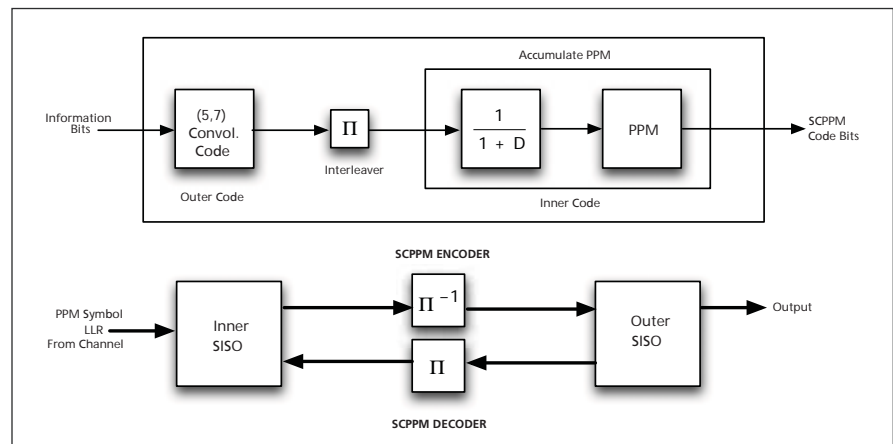


The **SCPPM Decoder** is designed according to a decoding algorithm that includes interleaving and de-interleaving algorithms in conjunction with SISO subalgorithms for decoding inner and outer codes.

module, and an interleaver connected in a loop (see figure). Each SISO module applies the Bahl-Cocke-Jelinek-Raviv (BCJR) algorithm to compute *a-posteriori* bit log-likelihood ratios (LLRs) from *a-priori* LLRs by traversing the code trellis in forward and backward directions. The SISO modules iteratively refine the LLRs by passing the estimates between one another much like the working of a turbine engine. Extrinsic information (the difference between the *a-posteriori* and *a-priori* LLRs) is exchanged rather than the *a-posteriori* LLRs to minimize undesired feedback. All computations are performed in the logarithmic domain, wherein multiplications are translated into additions, thereby reducing complexity and sensitivity to fixed-point implementation round-off errors.

To lower the required memory for storing channel likelihood data and the amounts of data transfer between the decoder and the receiver, one can discard the majority of channel likelihoods, using only the remainder in operation of the decoder. This is accomplished in the receiver by transmitting only a subset consisting of the likelihoods that correspond to time slots containing the largest numbers of observed photons during each PPM symbol period. The assumed number of observed photons in the remaining time slots is set to the mean of a noise slot. In low background noise, the selection of a small subset in this manner results in only negligible loss.

Other features of the decoder design to reduce complexity and increase speed include (1) quantization of metrics in an efficient procedure chosen to incur no more than a small performance loss and (2) the use of the max-star function that allows sum of exponentials to be computed by simple operations that involve only an addition, a subtraction, and a table lookup. Another prominent feature of the design is a provision for access to interleaver and de-interleaver memory in a single clock cycle, eliminating the multiple clock-cycle latency characteristic of prior interleaver and de-interleaver designs.

# Software

## Symbolic Processing Combined With Model-Based Reasoning

A computer program for the detection of present and prediction of future discrete states of a complex, real-time engineering system utilizes a combination of symbolic processing and numerical model-based reasoning. One of the biggest weaknesses of a purely symbolic approach is that it enables prediction of only future discrete states while missing all unmodeled states or leading to incorrect identification of an unmodeled state as a modeled one. A purely numerical approach is based on a combination of statistical methods and mathematical models of the applicable physics and necessitates development of a complete model to the level of fidelity required for prediction. In addition, a purely numerical approach does not afford the ability to qualify its results without some form of symbolic processing.

The present software implements numerical algorithms to detect unmodeled events and symbolic algorithms to predict expected behavior, correlate the expected behavior with the unmodeled events, and interpret the results in order to predict future discrete states. The approach embodied in this software differs from that of the BEAM methodology (aspects of which have been discussed in several prior *NASA Tech Briefs* articles), which provides for prediction of future measurements in the continuous-data domain.

*This program was written by Mark James of Caltech for NASA's Jet Propulsion Laboratory. Further information is contained in a TSP (see page 1).*

*This software is available for commercial licensing. Please contact Karina Edmonds of the California Institute of Technology at (626) 395-2322. Refer to NPO-45172.*

## Presentation Extensions of the SOAP

A set of extensions of the Satellite Orbit Analysis Program (SOAP) enables simultaneous and/or sequential presentation of information from multiple sources. SOAP is used in the aerospace community as a means of collaborative visualization and analysis of data on planned spacecraft missions. The following definitions of terms also describe the display modalities of SOAP as now extended: In SOAP terminology,

- "View" signifies an animated three-dimensional (3D) scene, two-dimensional still image, plot of numerical data, or any other visible display derived from a computational simulation or other data source;
- "Viewport" signifies a rectangular portion of a computer-display window containing a view;
- "Palette" signifies a collection of one or more viewports configured for simultaneous (split-screen) display in the same window;
- "Slide" signifies a palette with a beginning and ending time and an animation time step; and
- "Presentation" signifies a prescribed sequence of slides.

For example, multiple 3D views from different locations can be crafted for simultaneous display and combined with numerical plots and other representations of data for both qualitative and quantitative analysis. The resulting sets of views can be temporally sequenced to convey visual impressions of a sequence of events for a planned mission.

*This work was done by Robert Carnright of Caltech and David Stodden and John Coggi of The Aerospace Corporation for NASA's Jet Propulsion Laboratory.*

*This software is available for commercial licensing. Please contact Karina Edmonds of the California Institute of Technology at (626) 395-2322. Refer to NPO-45058.*

## Spreadsheets for Analyzing and Optimizing Space Missions

XCALIBR (XML Capability Analysis LIBRary) is a set of Extensible Markup Language (XML) database and spreadsheet-based analysis software tools designed to assist in technology-return-on-investment analysis and optimization of technology portfolios pertaining to outer-space missions. XCALIBR is also being examined for use in planning, tracking, and documentation of projects. An XCALIBR database contains information on mission requirements and technological capabilities, which are related by use of an XML taxonomy. XCALIBR incorporates a standardized interface for exporting data and analysis templates to an Excel spreadsheet. Unique features of XCALIBR include the following:

- It is inherently hierarchical by virtue of its XML basis.
- The XML taxonomy codifies a comprehensive data structure and data dictionary that includes performance metrics for spacecraft, sensors, and spacecraft systems other than sensors. The taxonomy contains >700 nodes representing all levels, from system through subsystem to individual parts.
- All entries are searchable and machine readable.
- There is an intuitive Web-based user interface.
- The software automatically matches technologies to mission requirements.
- The software automatically generates, and makes the required entries in, an Excel return-on-investment analysis software tool.
- The results of an analysis are presented in both tabular and graphical displays.

*This program was written by Raphael R. Some, Anil K. Agrawal, Akos J. Czikmantory, Charles R. Weisbin, and Hook Hua of Caltech and Jon M. Neff, Mark A. Cowdin, Brian S. Lewis, Juana Iroz, and Rick Ross of The Aerospace Corp. for NASA's Jet Propulsion Laboratory. Further information is contained in a TSP (see page 1).*

*This software is available for commercial licensing. Please contact Karina Edmonds of the California Institute of Technology at (626) 395-2322. Refer to NPO-41911.*

## Processing Ocean Images To Detect Large Drift Nets

A computer program processes the digitized outputs of a set of downward-looking video cameras aboard an aircraft flying over the ocean. The purpose served by this software is to facilitate the detection of large drift nets that have been lost, abandoned, or jettisoned. The development of this software and of the associated imaging hardware is part of a larger effort to develop means of detecting and removing large drift nets before they cause further environmental damage to the ocean and to shores on which they sometimes impinge.

The software is capable of near-real-time processing of as many as three video feeds at a rate of 30 frames per second. After a user sets the parameters of an adjustable algorithm, the software analyzes each video stream, detects any anomaly, issues a command to point a high-resolution camera toward the location of the anomaly, and, once the camera has been so aimed, issues a command to trigger the camera shutter. The resulting high-resolution image is digitized, and the resulting data are automatically uploaded to the operator's computer for analysis.

*This program was written by Tim Veenstra of Airborne Technologies Inc. for Stennis Space Center.*

*Inquiries concerning rights for its commercial use should be addressed to:*

*Tim Veenstra*
*Airborne Technologies Inc.*
*4338 N. Gunflint Trail*
*Wasilla, AK 99656*
*Phone: (907) 357-1500*
*Fax: (361) 825-5848*
*Email: tveenstra@atiak.com*
*Refer to SSC-00300-1, volume and number of this* NASA Tech Briefs *issue, and the page number.*

# Alternative Packaging for Back-Illuminated Imagers

**Electrical contacts are made accessible from the back side.**

*NASA's Jet Propulsion Laboratory, Pasadena, California*

An alternative scheme has been conceived for packaging of silicon-based back-illuminated, back-side-thinned complementary metal oxide/semiconductor (CMOS) and charge-coupled-device image-detector integrated circuits, including an associated fabrication process. This scheme and process are complementary to those described in "Making a Back-Illuminated Imager With Back-Side Connections" (NPO-42839), *NASA Tech Briefs*, Vol. 32, No. 7 (July 2008), page 38.

To avoid misunderstanding, it should be noted that in the terminology of imaging integrated circuits, "front side" or "back side" does not necessarily refer to the side that, during operation, faces toward or away from a source of light or other object to be imaged. Instead, "front side" signifies that side of a semiconductor substrate upon which the pixel pattern and the associated semiconductor devices and metal conductor lines are initially formed during fabrication, and "back side" signifies the opposite side. If the imager is of the type called "back-illuminated," then the back side is the one that faces an object to be imaged.

Initially, a back-illuminated, back-side-thinned image-detector is fabricated with its back side bonded to a silicon handle wafer. At a subsequent stage of fabrication, the front side is bonded to a glass wafer (for mechanical support) and the silicon handle wafer is etched away to expose the back side. The front-side integrated circuitry includes metal input/output contact pads, which are rendered inaccessible by the bonding of the front side to the glass wafer. Hence, one of the main problems is to make the input/output contact pads accessible from the back side, which is ultimately to be the side accessible to the external world. The present combination of an alternative packaging scheme and associated fabrication process constitute a solution of the problem.

The divergence between the alternative packaging scheme and fabrication process and prior such schemes and processes begins at the stage at which the integrated circuitry has been fabricated on the front side and the handle substrate is still attached. First, an outer oxide layer on the front side as fabricated thus far is planarized, then bonded to the glass wafer, as shown in the upper part of the figure. The remainder of the process can be summarized as follows. Through multiple steps of patterning, etching, and deposition, holes are formed in the silicon integrated-circuit substrate from the back side to expose metal traces and thereby form back-side contact pads. An ancillary benefit of the selective etching to expose the metal traces is that it cleans the exposed back surfaces of the traces, thereby making it possible to achieve low-resistance contact. Additional contact pads for electrical biasing of the silicon device substrate are also formed on the back side. The lower part of the figure depicts the finished product.
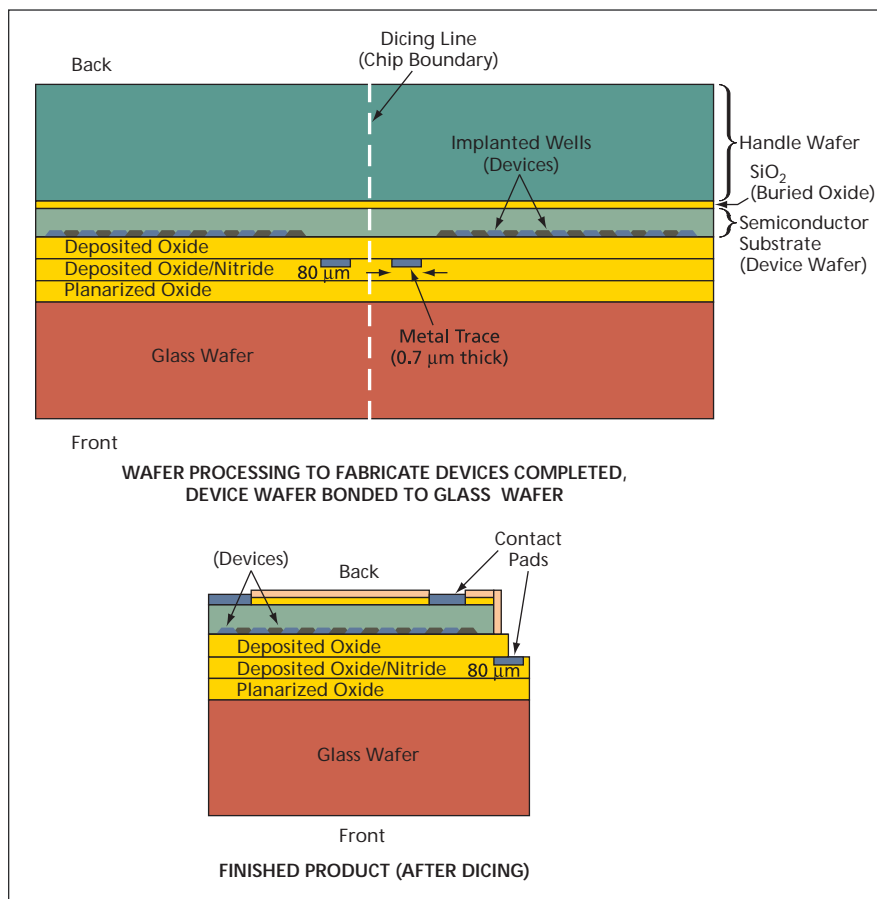
**These Simplified Cross Sections** depict an intermediate stage and the final stage in the fabrication of an imager according to the alternative scheme described in the text.

# Diamond Machining of an Off-Axis Biconic Aspherical Mirror
## Complex shapes can be produced at relatively low costs.

*Goddard Space Flight Center, Greenbelt, Maryland*

Two diamond-machining methods have been developed as part of an effort to design and fabricate an off-axis, biconic ellipsoidal, concave aluminum mirror for an infrared spectrometer at the Kitt Peak National Observatory. Beyond this initial application, the methods can be expected to enable satisfaction of requirements for future instrument mirrors having increasingly complex (including asymmetrical), precise shapes that, heretofore, could not readily be fabricated by diamond machining or, in some cases, could not be fabricated at all.

In the initial application, the mirror is prescribed, in terms of Cartesian coordinates $x$ and $y$, by aperture dimensions of 94 by 76 mm, placements of –2 mm off axis in $x$ and 227 mm off axis in $y$, an $x$ radius of curvature of 377 mm, a $y$ radius of curvature of 407 mm, an $x$ conic constant of 0.078, and a $y$ conic constant of 0.127. The aspect ratio of the mirror blank is about 6.

One common, "diamond machining" process uses single-point diamond turn-ing (SPDT). However, it is impossible to generate the required off-axis, biconic ellipsoidal shape by conventional SPDT because (1) rotational symmetry is an essential element of conventional SPDT and (2) the present off-axis biconic mirror shape lacks rotational symmetry. Following conventional practice, it would be necessary to make this mirror from a glass blank by computer-controlled polishing, which costs more than diamond machining and yields a mirror that is more difficult to mount to a metal bench.

One of the two present diamond-machining methods involves the use of an SPDT machine equipped with a fast tool servo (FTS). The SPDT machine is programmed to follow the rotationally symmetric asphere that best fits the desired off-axis, biconic ellipsoidal surface. The FTS is actuated in synchronism with the rotation of the SPDT machine to generate the difference between the desired surface and the best-fit rotationally symmetric asphere. In order to minimize the re-quired stroke of the FTS, the blanks were positioned at a large off-axis distance and angle, and the axis of the FTS was not parallel to the axis of the spindle of the SPDT machine. The spindle was rotated at a speed of 120 rpm, and the maximum FTS speed was 8.2 mm/s.

In the second diamond-machining method, the desired mirror surface is generated by raster fly-cutting on a multiaxis machine, all three Cartesian axes of which are actuated simultaneously. The diamond tool cuts through a mirror blank in a "down milling" mode with toric cutter compensation. In the original application, the fly-cut radius was 63 mm, the tool nose radius was 10 mm, and the finish cut lasted 16 hours.

*This work was done by Raymond G. Ohl of Goddard Space Flight Center, Werner Preuss of the University of Bremen, Alex Sohn of North Carolina State University, and John W. MacKenty of Space Telescope Science Institute. Further information is contained in a TSP (see page 1). GSC-14967-1*

# Laser Ablation Increases PEM/Catalyst Interfacial Area
## Increased interfacial area is expected to result in improved fuel-cell performance.

*NASA's Jet Propulsion Laboratory, Pasadena, California*

An investigational method of improving the performance of a fuel cell that contains a polymer-electrolyte membrane (PEM) is based on the concept of roughening the surface of the PEM, prior to deposition of a thin layer of catalyst, in order to increase the PEM/catalyst interfacial area and thereby increase the degree of utilization of the catalyst. The roughening is done by means of laser ablation under carefully controlled conditions. Next, the roughened membrane surface is coated with the thin layer of catalyst (which is typically platinum), then sandwiched between two electrode/catalyst structures to form a membrane/electrode assembly.

The feasibility of the roughening technique was demonstrated in experiments in which proton-conducting membranes made of a perfluorosulfonic acid-based hydrophilic, proton-conducting polymer were ablated by use
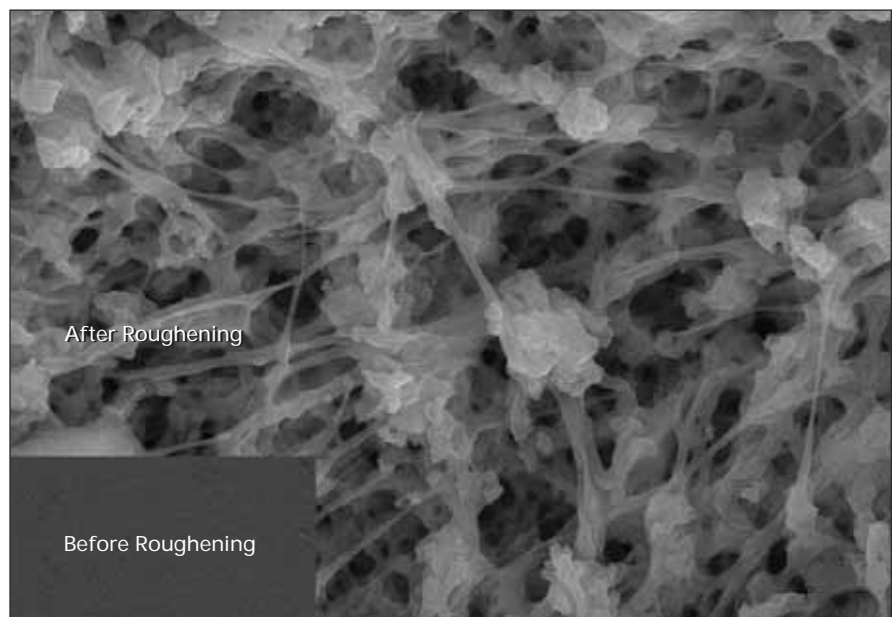


Figure 1. This **Scanning Electron Micrograph** shows portions of a PEM before and after roughening by laser ablation.
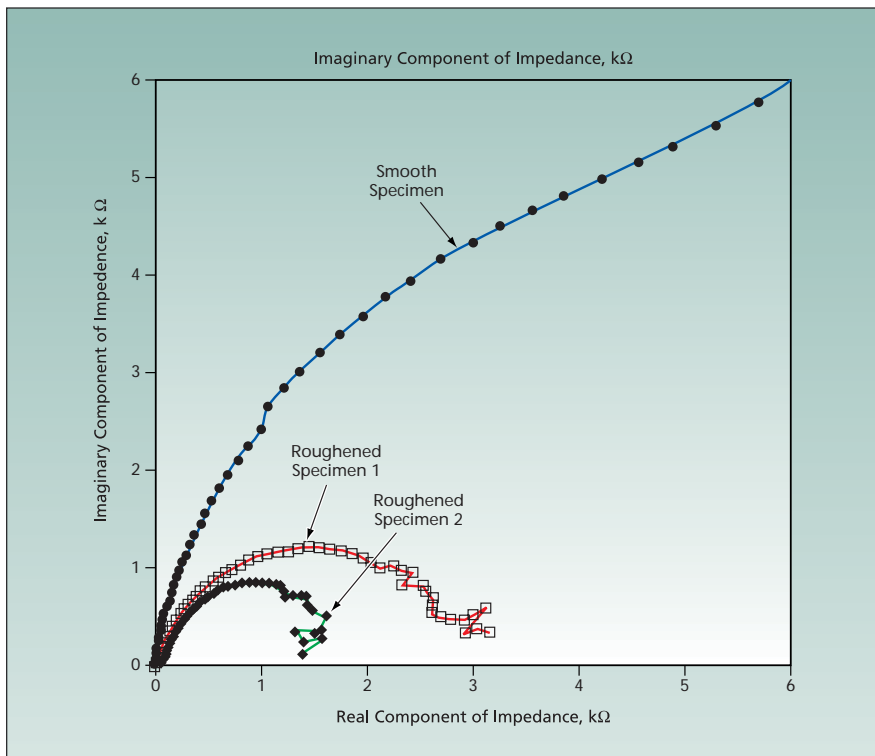
Figure 2. These **EIS Data** were acquired in measurements at frequencies from 100 kHz down to 10 mHz on 0.4-mm-thick smooth and roughened PEMs that had lateral dimensions of 3 by 3 mm, were 0.4 mm thick, and were coated with Pt on both faces. The smaller imaginary components of impedance of the roughened specimens are attributed to greater capacitances, which, in turn, are attributed to greater surface areas. Roughened specimens 1 and 2 were subjected to different laser-ablation conditions.

of femtosecond laser pulses. It was found that when proper combinations of the pulse intensity, pulse-repetition rate, and number of repetitions was chosen, the initially flat, smooth membrane surfaces became roughened to such an extent as to be converted to networks of nodules interconnected by filaments (see Figure 1).

In further experiments, electrochemical impedance spectroscopy (EIS) was performed on a pristine (smooth) membrane and on two laser-roughened membranes after the membranes were coated with platinum on both sides. Some preliminary EIS data were interpreted as showing that notwithstanding the potential for laser-induced damage, the bulk conductivities of the membranes were not diminished in the roughening process. Other preliminary EIS data (see Figure 2) were interpreted as signifying that the surface areas of the laser-roughened membranes were significantly greater than those of the smooth membrane. Moreover, elemental analyses showed that the sulfur-containing molecular groups necessary for proton conduction remained intact, even near the laser-roughened surfaces. These preliminary results can be taken as indications that laser-roughened PEMs should function well in fuel cells and, in particular, should exhibit current and power densities greater than those attainable by use of smooth membranes.

*This work was done by Jay Whitacre of Caltech and Steve Yalisove of the University of Michigan for NASA's Jet Propulsion Laboratory. Further information is contained in a TSP (see page 1). NPO-45075*

# Materials

## Damage Detection and Self-Repair in Inflatable/Deployable Structures

**Integrated sensors and self-repairing materials provide structural health management.**

*NASA's Jet Propulsion Laboratory, Pasadena, California*

Inflatable/deployable structures are under consideration for applications as varied as expansion modules for the International Space Station to destinations for space tourism to habitats for the lunar surface. Monitoring and maintaining the integrity of the physical structure is critical, particularly since these structures rely on non-traditional engineering materials such as fabrics, foams, and elastomeric polymers to provide the primary protection for the human crew. The closely related prior concept of monitoring structural integrity by use of built-in or permanently attached sensors has been applied to structures made of such standard engineering materials as metals, alloys, and rigid composites. To effect monitoring of flexible structures comprised mainly of soft goods, however, it will be necessary to solve a different set of problems — especially those of integrating power and data-transfer cabling that can withstand, and not unduly interfere with, stowage and subsequent deployment of the structures. By incorporating capabilities for self-repair along with capabilities for structural health monitoring, successful implementation of these technologies would be a significant step toward semi-autonomous structures, which need little human intervention to maintain. This would not only increase the safety of these structures, but also reduce the inspection and maintenance costs associated with more conventional structures.

A series of proof-of-concept technology sensing and self-repair technologies have recently been developed and tested individually, for future integration into a full health management system for inflatable/deployable structures. With further development, these technologies could be applied individually or as part of an entire system, depending on the particular architecture of the structure or on the specific mission needs. The technologies include:

- Arrays of thin-film capacitive or inductive sensors, made of a flexible circuit material that can be integrated into an inflatable/deployable structure for use in detecting the location and extent of damage. Damage manifests itself as changes in inductance or capacitance in elements of the sensor array.
- Strain gauges made from thin films of amorphous silicon for monitoring the integrity of thin, flexible structures. To reduce the amount of wiring required, thin-film transistors are used to construct an addressable, matrixed array of sensors allowing selection and readout of specific sensors in the array.
- Wireless sensors and passive (no-power) radio-frequency identification sensor tags to provide additional sensing capabilities such as strain sensing, temperature sensing, and impact or leak detection, without the need for data and power cables.
- Self-repairing elastomeric materials (such as those used to construct the bladder of a habitat), which incorporate microcapsules filled with a monomer resin and a small amount of a polymerization catalyst. Upon damage to the material, some of the capsules burst and release the monomer, becoming polymerized after making contact with the embedded catalyst and thus effecting repair of the damage.
- Sensory and self-repair features will eventually be combined into the structure to effect a unified structural health maintenance system. Sensors will alert humans to initial damage and will monitor the self-repair process, to indicate whether there is a need for human intervention for inspection and/or repair.

## Polyimide/Glass Composite High-Temperature Insulation

**This composite was found to exhibit an unexpectedly high degree of fire resistance.**

*Langley Research Center, Hampton, Virginia*

Lightweight composites of RP46 polyimide and glass fibers have been found to be useful as extraordinarily fire-resistant electrical-insulation materials. RP46 is a polyimide of the polymerization of monomeric reactants (PMR) type, developed by NASA Langley Research Center. RP46 has properties that make it attractive for use in electrical insulation at high temperatures. These properties include high-temperature resistance, low relative permittivity, low dissipation factor, outstanding mechanical properties, and excellent resistance to moisture and chemicals. Moreover, RP46 contains no halogen or other toxic materials and when burned it does not produce toxic fume or gaseous materials.

The U. S. Navy has been seeking lightweight, high-temperature-resistant elec-
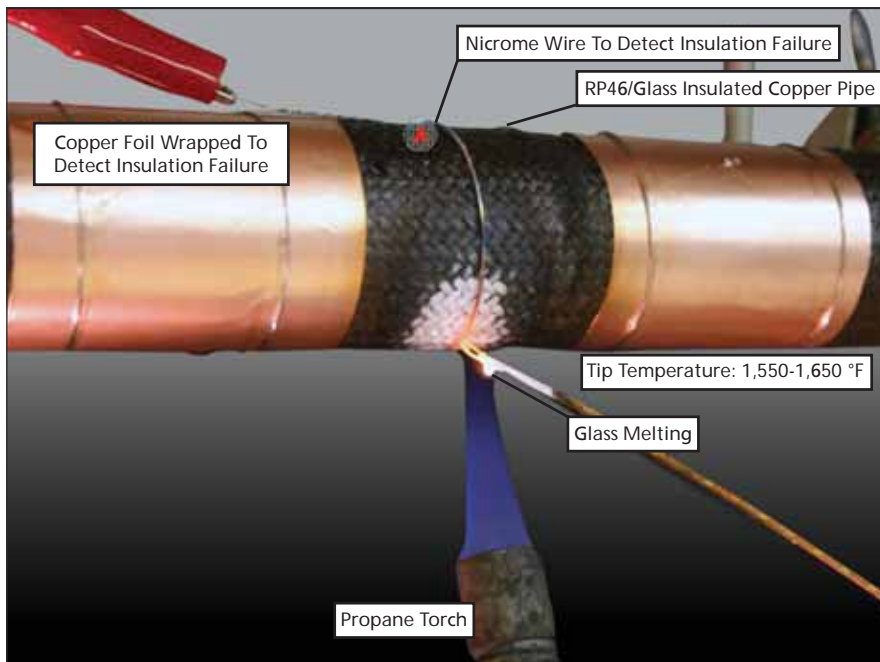
A **Gas Flame** at 1,600°F (about 871°C) was applied for 3 hours to a layer of RP46/glass composite 0.15 in. (about 3.8 mm) thick on a 1.62-in. (≈41.2-mm)-diameter copper pipe while a 60-Hz, 110-V alternating potential was applied across the layer. Electrical-insulation failure, effectively defined for the purpose of the test as being manifested by a current ≥0.25 A through the insulation, was not observed.

trical-insulation materials in a program directed toward reducing fire hazards and weights in ship electrical systems. To satisfy the requirements of this program, an electrical-insulation material must withstand a 3-hour gas-flame test at 1,600°F (about 871°C). Prior to the development reported here, RP46 was rated for use at temperatures from –150 to +700°F (about –101 to 371°C), and no polymeric product — not even RP46 — was expected to withstand the Navy 3-hour gas-flame test.

A typical process for applying RP46/glass-fiber composite to a wire, pipe, or other electrically conductive object that one seeks to insulate consists of the following steps:

1. The surface to be coated with the composite is prepared by roughening it, then cleaning it using methanol and acetone.
2. The roughened, cleaned surface is wrapped with either a prepreg [glass fabric or one or more layer(s) of glass fibers pre-impregnated with RP46] or a dry fabric or fiber sleeve or preform to a desired thickness.
3. If a dry sleeve has been wrapped, then at this point, it is infused with a resin solution having a suitable viscosity, by use of a vacuum-assisted resin-transfer molding (VARTM) technique. The VARTM step can be performed at either room temperature or an elevated temperature, depending on the specific resin solution used.
4. The workpiece as processed thus far is placed in an autoclave, wherein the resin is cured at an appropriate elevated temperature and pressure. If the resin has a low and stable melt viscosity, then the cure can be performed in a vacuum bag in an oven.

The figure depicts the Navy gas-flame test being performed on a copper pipe insulated with an RP46/glass-fiber composite. The same test was also performed on a similarly insulated aluminum pipe. The RP46/glass-fiber composite layers unexpectedly passed the tests, retaining their electrical-insulation integrity for more than 3 hours at 1,600±50°F (about 871±28°C). Furthermore, the composite showed remarkably high insulating capability. This was evident from the observation that while the RP46 was exposed to a temperature of 1,667°F (908°C), the temperature of the insulated conductor was only 229°F (109°C).

*This work was done by Ruth H. Pater, Peter Vasquez, Richard L. Chattin, Donald L. Smith, Thomas J. Skalski, and Gary S. Johnson of Langley Research Center and Sang-Hyon Chu of the National Institute of Aerospace. Further information is contained in a TSP (see page 1). LAR-17321-1*

# Nanocomposite Strain Gauges Having Small TCRs

**Usefully large gauge factors and acceptably small drifts should also be attainable.**

*John H. Glenn Research Center, Cleveland, Ohio*

Ceramic strain gauges in which the strain-sensitive electrically conductive strips made from nanocomposites of noble metal and indium tin oxide (ITO) are being developed for use in gas turbine engines and other power-generation systems in which gas temperatures can exceed 1,500°F (about 816°C). In general, strain gauges exhibit spurious thermally induced components of response denoted apparent strain. When temperature varies, a strain-gauge material that has a nonzero temperature coefficient of resistance (TCR) exhibits an undesired change in electrical resistance that can be mistaken for the change in resistance caused by a change in strain. It would be desirable to formulate strain-gauge materials having TCRs as small as possible so as to minimize apparent strain.

Most metals exhibit positive TCRs, while most semiconductors, including ITO, exhibit negative TCRs. The present development is based on the idea of using the negative TCR of ITO to counter the positive TCRs of noble metals and of obtaining the benefit of the ability of both ITO and noble metals to endure high temperatures. The noble metal used in this development thus far has been platinum. Combinatorial libraries of many ceramic strain gauges containing nanocomposites of various proportions of ITO and platinum were fabricated by reactive co-sputtering from ITO and platinum targets onto alumina- and zirconia-based substrates mounted at various positions between the targets. TCR values of the sensors were determined from measurements made in thermal cycling between room
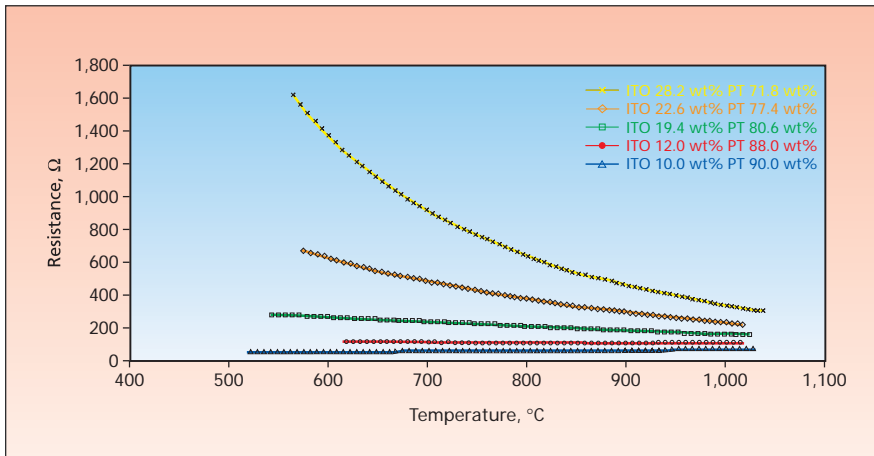
The **TCRs** (slopes of electrical resistance versus temperature) of five platinum/ITO nanocomposite films having different compositions ranged from negative to near zero to slightly positive, suggesting that it should be possible to formulate platinum/ITO composites having TCRs very close to zero.

temperature and 1,000°C. Piezoresistive responses of the sensors were measured at strain levels up to $10^{-3}$ at temperatures from room temperature to 1,200°C.

The chemical compositions of the most promising combinatorial libraries were analyzed by energy-dispersive x-ray spectrometry and scanning electron microscopy. Preliminary results (see fig-

ure) have been interpreted as indicating that TCRs near zero, from room temperature to 1,000°C, could be achieved even in non-optimized platinum/ITO nanocomposite strain gauges containing approximately 12 weight percent of ITO. For one such strain gauge, the gauge factor was found to be relatively large (≈26) and the drift rate very low (0.018 percent/h). On the basis of these and similar results, other combinatorial libraries of composites of ITO with Pd, Ni, NiCoCrAlY alloys, W, and Ir are also under consideration.

# ❁ Quick-Connect Windowed Non-Stick Penetrator Tips for Rapid Sampling

*NASA's Jet Propulsion Laboratory, Pasadena, California*

Standard penetrator sampling systems were designed in order to allow for sampling via penetrators to produce a full set of sample acquisitions including volatile liquids, fine powders, and solid fragments. A gravity harpoon sampler has been designed with a removable tip and a quick coupling. The separation allows for sample handling and eliminates sample cross-contamination. Also, this design allows for multiple use of the penetrator body, which is the largest and heaviest part of the penetrator, while allowing for multiple changes of the light-mass, penetrator tip to avoid sample cross-contamination.

The penetrator tip design has been improved by adding a spring trap to retain the sample, as well as a means for connecting to a quick coupling. Quick connect tips have been demonstrated in a sample handling carousel. The penetrator was released and rewound and the tips were released into a circular platter for rotation into instrument stations. The pyro-harpoon sampler was fabricated and tested with a NASA Standard Initiator (NSI) pyrotechnic charge. Initial tests collected cryogenic ice, but removal of the small pyro-harpoon from the ice was difficult. A brass metal sheath was then fitted over the harpoon tip, and removal from the ice was greatly alleviated by leaving the sheath in the ice. Quartz windows in the tips allow direct optical and spectral imaging and gas chromatography-mass spectrometer (GCMS) pyrolysis, and were found to survive impact. All systems were successfully tested by dropping into sand and into cryogenic ice.

*This work was done by Stewart Sherrit, Jack A. Jones, and Mircea Badescu of Caltech for NASA's Jet Propulsion Laboratory. Further information is contained in a TSP (see page 1). NPO-45861*

# ❁ Modeling Unsteady Cavitation and Dynamic Loads in Turbopumps

**Magnitudes and frequencies of cavitation-instability-induced loads can be estimated.**

*Marshall Space Flight Center, Alabama*

A computational fluid dynamics (CFD) model that includes representations of effects of unsteady cavitation and associated dynamic loads has been developed to increase the accuracy of simulations of the performances of turbopumps. Although the model was originally intended to serve as a means of analyzing preliminary designs of turbopumps that supply cryogenic propellant liquids to rocket engines, the model could also be applied to turbopumping of other liquids: this can be considered to have been already demonstrated, in that the validation of the model was performed by comparing results of simulations performed by use of the model with results of sub-scale experiments in water.

The need for this or a similar model arises as follows: Cavitation instabilities in a turbopump are generated as inlet pressure drops and vapor cavities grow on inducer blades, eventually becoming unsteady. The unsteady vapor cavities lead to rotation cavitation, in which the cavities detach from the blades and become part of a fluid mass that rotates relative to the inducer, thereby generating a fluctuating load. Other instabilities (e.g., surge instabilities) can couple with cavitation instabilities, thereby compounding the deleterious effects of unsteadiness on other components of the fluid-handling system of which the turbopump is a part and thereby, further, adversely affecting the mechanical integrity and safety of the system.

Therefore, an ability to predict cavitation-instability-induced dynamic pressure loads on the blades, the shaft, and other pump parts would be valuable in helping to quantify safe margins of inducer operation and in contributing to understanding of design compromises. Prior CFD models do not afford this ability. Heretofore, the primary parameter used in quantifying cavitation performance of a turbopump inducer has been the critical suction specific speed at which head breakdown occurs. This parameter is a mean quantity calculated on the basis of assumed steady-state operation of the inducer; it does not account for dynamic pressure loads associated with unsteady flow caused by instabilities. Because cavitation instabilities occur well before mean breakdown in inducers, engineers have, until now, found it necessary to use conservative factors of safety when analyzing the results of numerical simulations of flows in turbopumps.

The model has been implemented within CRUNCH CFD, which is a proprietary CFD computer program that has been extensively tested and validated for predicting mean pump performances. The provision of the capability to simulate cavitation instabilities involved two major enhancements of CRUNCH CFD: (1) incorporation of a capability to model the varying properties of real cryogenic fluids in the presence of cavitation and (2) development of more-sophisticated physical submodels that, in comparison with corresponding prior models, represent more accurately the rates at which vapors are created or condensed back to liquids.

The model has been demonstrated to provide accurate estimates of the magni-

tudes and frequencies of unsteady pressure loads on inducer blades. The model has also been demonstrated to enable estimation of loads on pump shafts and bearings. The ability to estimate these loads is important because (1) it is difficult to measure such loads in experiments and (2) a high load on a shaft can cause an inducer to rub against the shroud that houses the pump and, in the worst case, can result in seizing or in failure of the shaft.

# Continuous-Flow System Produces Medical-Grade Water

**Pressurized flowing water is heated by absorption of microwave power.**

*John H. Glenn Research Center, Cleveland, Ohio*

A continuous-flow system utilizes microwave heating to sterilize water and to thermally inactivate endotoxins produced in the sterilization process. The system is designed for use in converting potable water to medical-grade water. Systems like this one could be used for efficient, small-scale production of medical-grade water in laboratories, clinics, and hospitals. This system could be adapted to use in selective sterilization of connections in ultra-pure-water-producing equipment and other equipment into which intrusion by microorganisms cannot be tolerated. Lightweight, portable systems based on the design of this system could be rapidly deployed to remote locations (e.g., military field hospitals) or in response to emergencies in which the normal infrastructure for providing medical-grade water is disrupted. Larger systems based on the design of this system could be useful for industrial production of medical-grade water.

The basic microwave-heating principle of this system is the same as that of a microwave oven: An item to be heated, made of a lossy dielectric material (in this case, flowing water) is irradiated with microwaves in a multimode microwave cavity. The heating is rapid and efficient because it results from absorption of microwave power throughout the volume of the lossy dielectric material.

In this system, a copper tube having a length of 49.5 cm and a diameter of 2.25 cm serves as both the microwave cavity and the sterilization chamber. Microwave power is fed via a coaxial cable to an antenna mounted inside the tube at mid-length (see figure). Efficient power transfer occurs due to the shift in wavelength associated with the high permittivity of water combined with the strong coupling of 2.45-GHz microwaves with rotational-vibrational transitions of the dipolar water molecule. The sterilization chamber is ther-
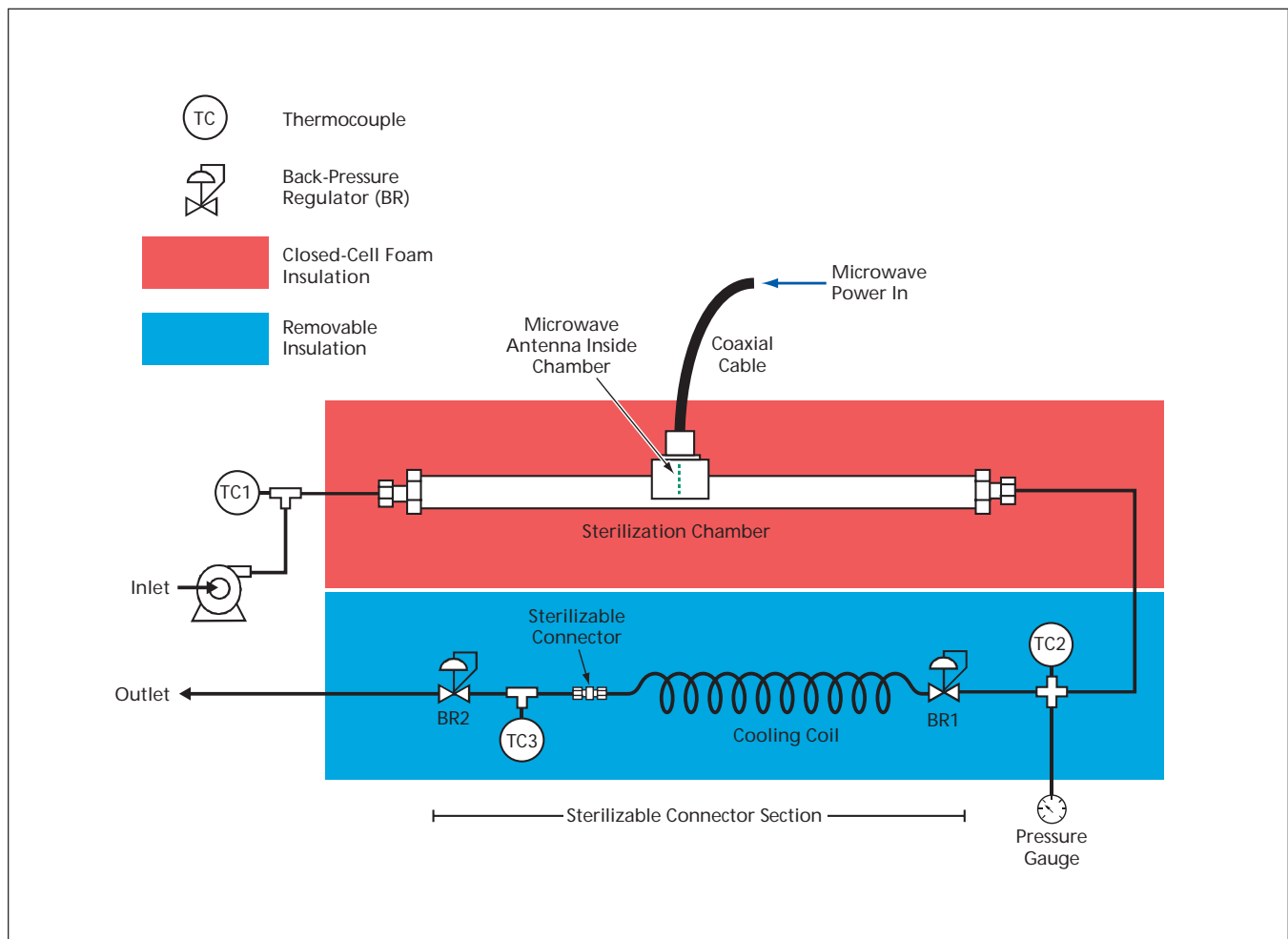


The **Sterilization Chamber** is a copper tube. A coaxial cable connects a microwave source to an antenna inside the chamber at mid-length. Downstream of the sterilization chamber, the sterilized water is cooled at reduced pressure.

mally insulated with closed-cell foam to reduce heat losses.

To enable a sufficiently high degree of sterilization and inactivation of endotoxins during the time of transit of water along the tube, it is necessary to heat the water to a temperature significantly above traditional autoclave temperatures. In order to do this, it is necessary to choose an appropriate combination of microwave power and flow rate, and to maintain the flowing water at a pressure high enough to prevent boiling at the desired maximum temperature. For example, typical steady-state operating conditions in experiments on this system included a flow rate of 13 mL/min, a pressure of 0.69 MPa, and a microwave power of 150 W, resulting in a sterilization temperature between 155 and 158 °C. Under these conditions, the system demonstrated effective sterilization and inactivation of endotoxins when challenged with influent water containing a mixed culture of *Bacillus stearothermophilus*, *E. coli*, and *Pseudomonas aeruginosa*.

Downstream of the sterilization chamber, the water is cooled at reduced pressure in a sterilizable connector section that contains a cooling coil situated between two pressure regulators. At the beginning of operation, for the purpose of sterilization, the sterilizable connector section is surrounded by removable insulation and maintained at full sterilization temperature and pressure using pressure regulator 2. For subsequent steady-state operation, insulation is removed from this section, causing the temperature to decline to the point where pressure regulator 2 can be opened to the atmosphere, requiring adjustment of pressure regulator 1 to maintain full sterilization pressure in the sterilization chamber.

# Discrimination of Spore-Forming Bacilli Using *spo*IVA

## Sporulation-specific primers are mixed into a PCR cocktail.

### NASA's Jet Propulsion Laboratory, Pasadena, California

A method of discriminating between spore-forming and non-spore-forming bacteria is based on a combination of simultaneous sporulation-specific and non-sporulation-specific quantitative polymerase chain reactions (Q-PCRs). The method was invented partly in response to the observation that for the purposes of preventing or reducing biological contamination affecting many human endeavors, ultimately, only the spore-forming portions of bacterial populations are the ones that are problematic (or, at least, more problematic than are the non-spore-forming portions).

In some environments, spore-forming bacteria constitute small fractions of the total bacterial populations. The use of sporulation-specific primers in Q-PCR affords the ability to assess the spore-forming fraction of a bacterial population present in an environment of interest. This assessment can provide a more thorough and accurate understanding of the bacterial contamination in the environment, thereby making it possible to focus contamination-testing, contamination-prevention, sterilization, and decontamination resources more economically and efficiently.

The method includes the use of sporulation-specific primers in the form of designed, optimized deoxyribonucleic acid (DNA) oligonucleotides specific for the bacterial *spo*IVA gene (see table). [In "*spo*IVA," "IV" signifies Roman numeral four and the entire quoted name refers to gene A for the fourth stage of sporulation.] These primers are mixed into a PCR cocktail with a given sample of bacterial cells. A control PCR cocktail into which are mixed universal 16S rRNA primers is also prepared. ["16S rRNA" denotes a ri-

| Primer and Probe Sequences for Discriminating and Quantifying Spore-Forming Bacteria | | |
| --- | --- | --- |
| **Primer Name** | **Position** | **Sequence** |
| SpoIVa382f | Forward Primer Sequence | 5'-TGA AGA GCC NAT YCC RTT-3' |
| SpoIVa752r | Reverse Primer Sequence | 5'-ACC ATT ACC CAG CTY GG-3' |
| **Primer and Probe Sequences for Discriminating and Quantifying *B. anthracis* Bacteria** | | |
| **Primer/Probe Name** | **Position** | **Sequence** |
| SpoIVa358f | Forward Primer Sequence | 5'-ACB CCW TGG TAY GAA GAR CC-3' |
| SpoIVa508r | Reverse Primer Sequence | 5'-TTC TGC CTC TAT ATA ATC TCT TCT TGG-3' |
| SpoIVa385f | Fluorescent Probe Sequence | 5'-TTC CAT GAA GCT GCA GAA ATC GG-Fluor-3' |

Note: A = adenosine; C = cytosine; T = tyrosine; G = guanine; N = the use of any of the 4 nucleotides, A, T, G, or C; R = the use of either purine nucleotide, A or G; W = the use of A or T; Y = the use of either pyrimidine nucleotide, C or T.

**These Primers** can be used, variously, for discriminating spore-forming bacteria in general or *Bacillus anthracis* in particular.

bosomal ribonucleic acid (rRNA) sequence that is common to all organisms.] Following several cycles of heating and cooling according to the PCR protocol to amplify amounts of DNA molecules, the amplification products can be analyzed to determine the types of bacterial cells present within the samples.

If the amplification product is strong, relative to the product of a control PCR sequence, then it is concluded that the bacterial population in the sample consists predominantly of spore-forming cells. If the amplification product is weak or nonexistent, then it is concluded that the bacterial population in the sample consists predominantly or entirely of non-spore-forming cells.

# Physical Sciences

# nBn Infrared Detector Containing Graded Absorption Layer

**Potential applications include environmental monitoring, firefighting, law enforcement, and medical diagnosis.**

*NASA's Jet Propulsion Laboratory, Pasadena, California*

It has been proposed to modify the basic structure of an nBn infrared photodetector so that a plain electron-donor-type (n-type) semiconductor contact layer would be replaced by a graded n-type III–V alloy semiconductor layer (i.e., ternary or quarternary) with appropriate doping gradient. The abbreviation "nBn" refers to one aspect of the unmodified basic device structure: There is an electron-barrier ("B") layer between two n-type ("n") layers, as shown in the upper part of the figure. One of the n-type layers is the aforementioned photon-absorption layer; the other n-type layer, denoted the contact layer, collects the photocurrent.

The basic unmodified device structure utilizes minority-charge-carrier conduction, such that, for reasons too complex to explain within the space available for this article, the dark current at a given temperature can be orders of magnitude lower (and, consequently, signal-to-noise ratios can be greater) than in infrared detectors of other types. Thus, to obtain a given level of performance, less cooling (and, consequently, less cooling equipment and less cooling power) is needed. [In principle, one could obtain the same advantages by means of a structure that would be called "pBp" because it would include a barrier layer between two electron-acceptor-type (p-type) layers.] The proposed modifications could make it practical to utilize nBn photodetectors in conjunction with readily available, compact thermoelectric coolers in diverse infrared-imaging applications that could include planetary exploration, industrial quality control, monitoring pollution, firefighting, law enforcement, and medical diagnosis.

The modifications are meant to address an aspect of the basic unmodified device structure that limits the performance advantages to photons having wavelengths less than either of two specific values: 3.4 or 4.4 μm. These values correspond to bandgaps associated with two specific semiconductor alloy com-

positions (InAs or InAsSb, respectively), either of which could be used in the photon-absorption layer. For reasons that, once again, are too complex to describe within the space available for this article, these two compositions are the only ones that afford the energy-band structures needed to obtain the desired combination of adequate

photogenerated current and reduction of dark current with AlSb barrier. For other values, depending on the type of energy-band alignment, there arise, in the B layer, a valence-band well for holes. Undesirably, holes will be trapped in the valence-band well, with consequent reduction of collectable hole photocurrent through tunneling
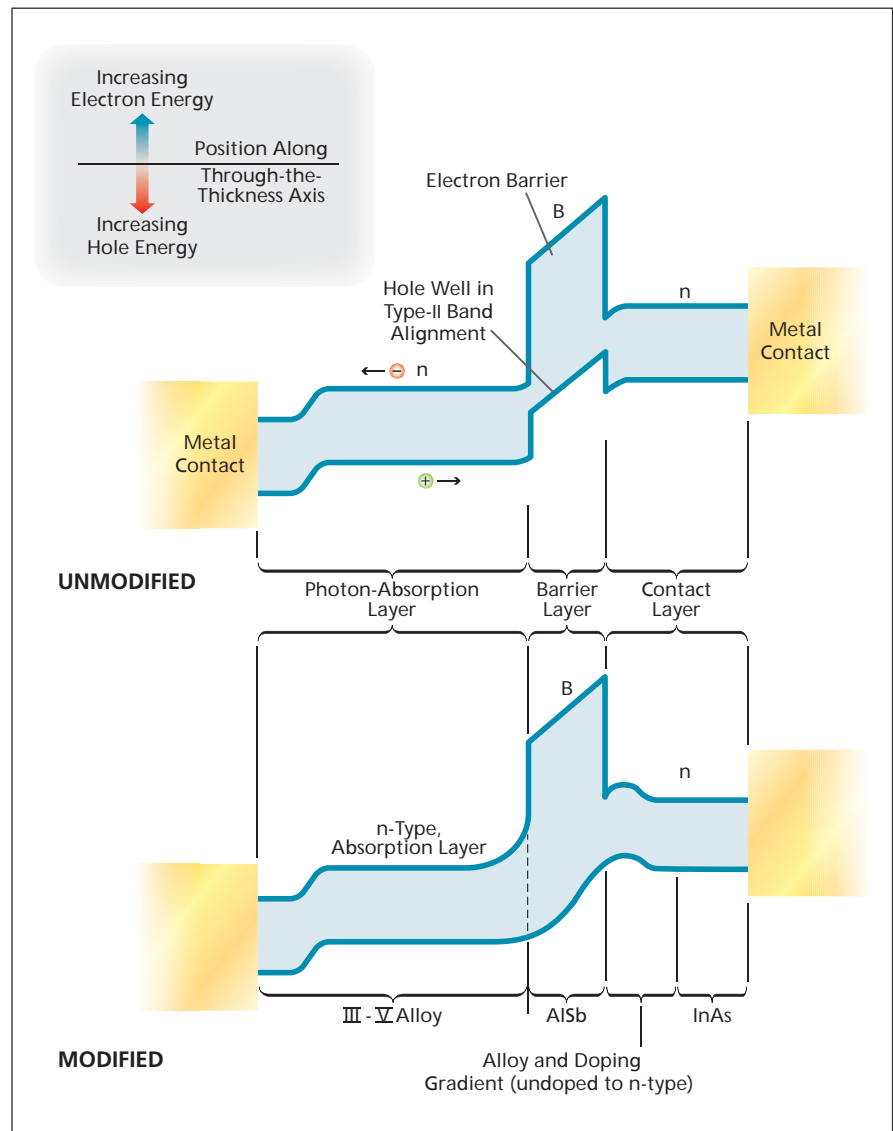


These **Energy-Band Diagrams**, simplified and not to scale, pertain to an example of an unmodified nBn photodetector and a corresponding modified nBn photodetector, both with bias applied via the metal contacts.

of holes to the conduction band and buildup of charge at the Bn (i.e., at the barrier and n-contact) interface.

The lower part of the figure depicts the energy-band structure for one of the proposed modified device structures. In this case, the plain n-type contact layer would be replaced with a graded III–V alloy layer with proper doping gradient from undoped to doped n contact. The valence band potential dip can be eliminated under proper bis condition. In a different modification, not shown in the figure, the plain photon-absorption layer could be replaced with a chirped strain-layer superlattice. In either modification, the graded or chirped structure would provide an energy ramp that would serve as a smooth path for transport of minority charge carriers. The valence-band hole trap and the associated undesired effects would be eliminated.

*This work was done by Sarath D. Gunapala, David Z. Ting, Cory J. Hill, and Sumith V. Bandara of Caltech for NASA's Jet Propulsion Laboratory.*

# Atomic References for Measuring Small Accelerations

## These systems may be used in military and geological applications.

*NASA's Jet Propulsion Laboratory, Pasadena, California*

Accelerometer systems that would combine the best features of both conventional (e.g., mechanical) accelerometers and atom interferometer accelerometers (AIAs) have been proposed. These systems are intended mainly for use in scientific research aboard spacecraft but may also be useful on Earth in special military, geological, and civil-engineering applications.

Conventional accelerometers can be sensitive, can have high dynamic range, and can have high frequency response, but they lack accuracy and long-term stability. AIAs have low frequency response, but they offer high sensitivity, and high accuracy for measuring small accelerations. In a system according to the proposal, a conventional accelerometer would be used to perform short-term measurements of higher-frequency components of acceleration, while an AIA would be used to provide consistent calibration of, and correction of errors in, the measurements of the conventional accelerometer in the lower-frequency range over the long term.

A brief description of an AIA is prerequisite to a meaningful description of a system according to the proposal. An AIA includes a retroreflector next to one end of a cell that contains a cold cloud of atoms in an ultrahigh vacuum. The atoms in the cloud are in free fall. The retroreflector is mounted on the object, the acceleration of which is to be measured. Raman laser beams are directed through the cell from the end opposite the retroreflector, then pass back through the cell after striking the retroreflector. The Raman laser beams together with the cold atoms measure the relative acceleration, through the readout of the AIA, between the cold atoms and the retroreflector.
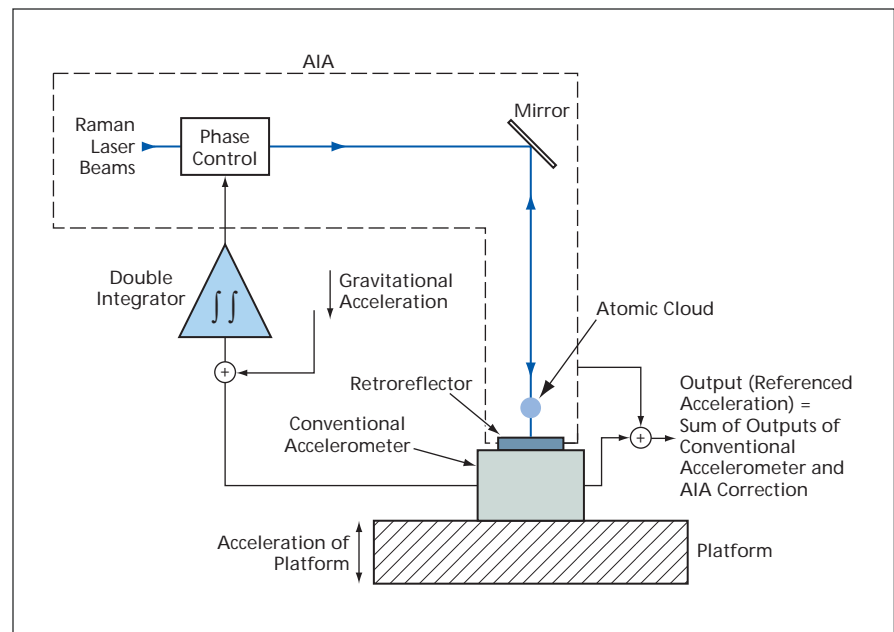


An **Atom-Interferometer Accelerometer** (AIA) and a conventional accelerometer would be connected in a feedback loop, such that the net acceleration measurement would be that of the conventional accelerometer plus a correction term provided by the AIA.

A system according to the proposal could be realized in several alternative implementations. In the simplest implementation (see figure), the conventional accelerometer and the retroreflector of the AIA would be mounted on a platform, the acceleration of which was to be measured. The phase of the Raman laser beams is frequency-chirped to remove the known gravity acceleration. From the output of the conventional accelerometer, the equivalent phase shift of the AIA is converted through the electronic double integrator. This phase is electronically fed forward to a Raman laser phase shifter such that it cancels out the phase shift in the AIA due to the acceleration read by the conventional accelerometer. The remaining part of the AIA phase shift would be used to compute a residual acceleration that would be applied as a correction to the acceleration measurement of the conventional accelerometer.

*This work was done by Lute Maleki and Nan Yu of Caltech for NASA's Jet Propulsion Laboratory. Further information is contained in a TSP (see page 1).*
NPO-43776

# Ultra-Broad-Band Optical Parametric Amplifier or Oscillator

**Potential applications include wavelength-multiplexing communications and generating reference frequencies.**

*NASA's Jet Propulsion Laboratory, Pasadena, California*

A concept for an ultra-broad-band optical parametric amplifier or oscillator has emerged as a by-product of a theoretical study in fundamental quantum optics. The study was originally intended to address the question of whether the two-photon temporal correlation function of light [in particular, light produced by spontaneous parametric down conversion (SPDC)] can be considerably narrower than the inverse of the spectral width (bandwidth) of the light. The answer to the question was found to be negative. More specifically, on the basis of the universal integral relations between the quantum two-photon temporal correlation and the classical spectrum of light, it was found that the lower limit of two-photon correlation time is set approximately by the inverse of the bandwidth. The mathematical solution for the minimum two-photon correlation time also provides the minimum relative frequency dispersion of the down-converted light components; in turn, the minimum relative frequency dispersion translates to the maximum bandwidth, which is important for the design of an ultra-broad-band optical parametric oscillator or amplifier.

In the study, results of an analysis of the general integral relations were applied in the case of an optically nonlinear, frequency-dispersive crystal in which SPDC produces collinear photons. Equations were found for the crystal orientation and pump wavelength, specific for each parametric-down-converting crystal, that eliminate the relative frequency dispersion of collinear degenerate (equal-frequency) signal and idler components up to the fourth order in the frequency-detuning param-
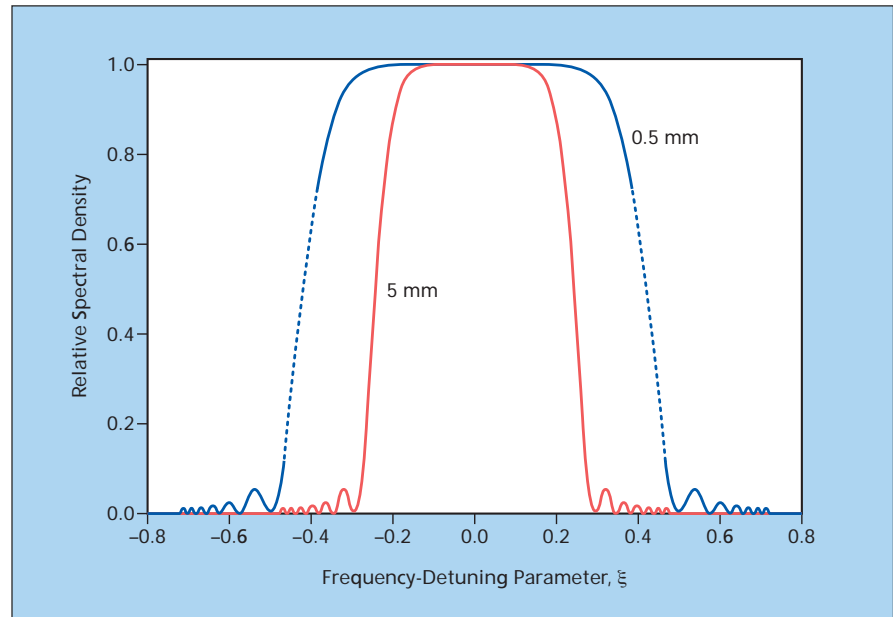


The **Relative Spectral Density in SPDC** was calculated for a suitably oriented pump beam in 5- and 0.5-mm-long $BeSO_4$ crystals for a degenerate wavelength of 923.8 nm.

eter, $\xi$. [The degenerate frequency, $\nu_0$, of the signal or idler component is half the pump frequency. If the difference between the signal or pump component and the degenerate frequency is $\nu$ (in which case the corresponding difference for the pump or signal component, respectively, is $-\nu$), then $\xi \equiv \nu/\nu_0$.]

As a result of the elimination of the relative frequency dispersion up to fourth order, an optical parametric amplifier consisting of such a crystal at the specified orientation and pumped at the specified wavelength can be designed to exhibit a relatively flat spectral-density-versus-frequency curve over more than an octave (see figure). Conveniently, the octave could be chosen to

include two wavelength bands — centered at 1,330 and 1,560 nm — that are used in optical communications. Hence, for example, the amplifier might be useful in a wavelength-multiplexing communication system using these two wavelength bands. In another potential application, by configuring this amplifier as a mode-locked oscillator, one could obtain a self-locked comblike spectrum that could serve as an excellent set of frequency references.

*This work was done by Dmitry Strekalov, Andrey Matsko, Anatoliy Savchenkov, and Lute Maleki of Caltech for NASA's Jet Propulsion Laboratory. For further information, contact iaoffice@jpl.nasa.gov.*
NPO-41584

# Particle-Image Velocimeter Having Large Depth of Field

**This instrument could be used to monitor particle-laden flows.**

*Goddard Space Flight Center, Greenbelt, Maryland*

An instrument that functions mainly as a particle-image velocimeter provides data on the sizes and velocities of flying opaque particles. The instrument is being developed as a means of characterizing fluxes of wind-borne dust particles

in the Martian atmosphere. The instrument could also adapted to terrestrial use in measuring sizes and velocities of opaque particles carried by natural winds and industrial gases. Examples of potential terrestrial applications include monitoring of airborne industrial pollutants and airborne particles in mine shafts.

The design of this instrument reflects an observation, made in field research, that airborne dust particles derived from soil and rock are opaque enough to be

observable by use of bright field illumination with high contrast for highly accurate measurements of sizes and shapes. The instrument includes a source of collimated light coupled to an afocal beam expander and an imaging array of photodetectors. When dust particles travel through the collimated beam, they cast shadows. The shadows are magnified by the beam expander and relayed to the array of photodetectors.

Inasmuch as the images captured by the array are of dust-particle shadows rather of the particles themselves, the depth of field of the instrument can be large: the instrument has a depth of field of about 11 mm, which is larger than the depths of field of prior particle-image velocimeters. The instrument can resolve, and measure the sizes and velocities of, particles having sizes in the approximate range of 1 to 300 μm.

For slowly moving particles, data from two image frames are used to calculate velocities. For rapidly moving particles, image smear lengths from a single frame are used in conjunction with particle-size measurement data to determine velocities.

# Enhancing SERS by Means of Supramolecular Charge Transfer
## Sensors based on this method could detect chemical and biological hazards.

*NASA's Jet Propulsion Laboratory, Pasadena, California*

In a proposed method of sensing small quantities of molecules of interest, surface enhanced Raman scattering (SERS) spectroscopy would be further enhanced by means of intermolecular or supramolecular charge transfer. There is a very large potential market for sensors based on this method for rapid detection of chemical and biological hazards.

In SERS, the Raman signals (vibrational spectra) of target molecules become enhanced by factors of the order of $10^8$ when those molecules are in the vicinities of nanostructured substrate surfaces that have been engineered to have plasmon resonances that enhance local electric fields. SERS, as reported in several prior *NASA Tech Briefs* articles and elsewhere, has remained a research tool and has not yet been developed into a practical technique for sensing of target molecules: this is because the short range (5 to 20 nm) of the field enhancement necessitates engineering of receptor molecules to attract target molecules to the nanostructured substrate surfaces and to enable reliable identification of the target molecules in the presence of interferants.

Intermolecular charge-transfer complexes have been used in fluorescence-, photoluminescence-, and electrochemistry-based techniques for sensing target molecules, but, until now, have not been considered for use in SERS-based sensing. The basic idea of the proposed method is to engineer receptor molecules that would be attached to nanostructured SERS substrates and that would interact with the target molecules to form receptor-target supramolecular charge-transfer complexes wherein the charge transfer could be photoexcited.

As shown schematically in the figure,



**Photoexcitation of Charge-Transfer Resonance**

**T Molecule attracted to R Molecule**

**R-T Charge-Transfer Complex Having Resonance at λ₁**

**Release of T Through Electrochemical Reduction**

**Plasmon and Supramolecular Electronic Resonance Spectra**
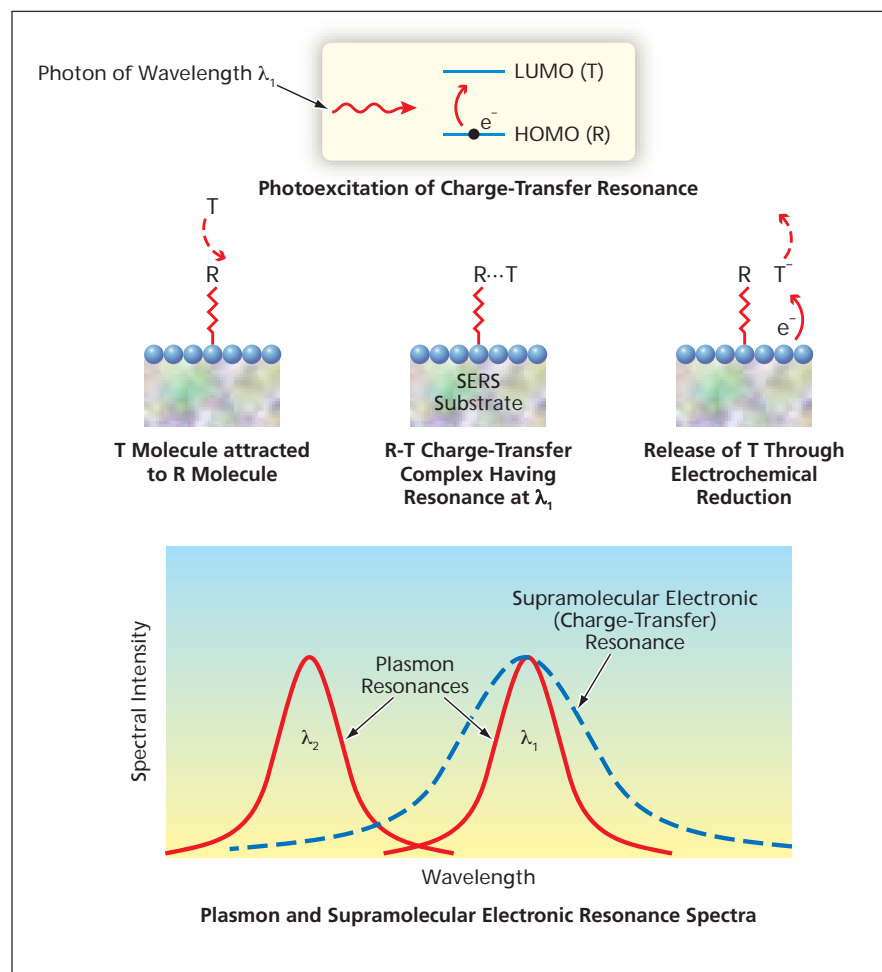
A **Target Molecule Would Become Bound** to a receptor molecule on an SERS substrate. The resulting R-T complex would have a charge-transfer energy band that would coincide with a plasmon resonance, $\lambda_1$, of the substrate. Optionally, the target molecule could be released through electrochemical reduction.

a SERS substrate would be functionalized with a receptor (R) molecule that has an affinity for a target (T) molecule. The receptor molecule could be designed so that the lowest unoccupied molecular orbital (LUMO) of the target molecule would lie above the highest occupied molecular orbital (HOMO) of the target molecule by an energy difference that would correspond to one of

the plasmon resonances of the SERS. Conversely, the plasmon of the SERS substrate could be tailored so that its resonance would lie in the charge-transfer energy band of the R-T complex. In addition to the aforesaid factor-of-$10^8$ SERS enhancement, there would be an additional enhancement, by a factor of the order of $10^3$ to $10^6$, contributed by the vibronic energy levels associated with the charge transfer.

With this further enhancement, the detection principle is a form of surface enhanced resonance Raman scattering (SERRS) spectroscopy. The resulting Raman spectrum would consist of a mixture of SERS vibrational peaks from R and T as well more intense SERRS peaks associated with R and T modes that participate in the charge transfer. These strong charge-transfer peaks would enable discrimination of important target molecules from interferants that may also be SERS-active. The sensor/molecule system as described thus far would potentially be reversible in the sense that the R-T interactions could be turned off by applying a bias voltage to electrochemically reduce T to T-. Because T- would no longer have an affinity for R, T could be easily washed away.

*This work was done by Eric Wong of Caltech, Amar Flood of the Indiana University Bloomington, and Alfredo Morales of Sandia*

# Improving 3D Wavelet-Based Compression of Hyperspectral Images
## Detrimental effects of spectral ringing are reduced or eliminated.

*NASA's Jet Propulsion Laboratory, Pasadena, California*

Two methods of increasing the effectiveness of three-dimensional (3D) wavelet-based compression of hyperspectral images have been developed. (As used here, "images" signifies both images and digital data representing images.) The methods are oriented toward reducing or eliminating detrimental effects of a phenomenon, referred to as spectral ringing, that is described below.

In 3D wavelet-based compression, an image is represented by a multiresolution wavelet decomposition consisting of several subbands obtained by applying wavelet transforms in the two spatial dimensions corresponding to the two spatial coordinate axes of the image plane, and by applying wavelet transforms in the spectral dimension. Spectral ringing is named after the more familiar spatial ringing (spurious spatial oscillations) that can be seen parallel to and near edges in ordinary images reconstructed from compressed data. These ringing phenomena are attributable to effects of quantization. In hyperspectral data, the individual spectral bands play the role of edges, causing spurious oscillations to occur in the spectral dimension. In the absence of such corrective measures as the present two methods, spectral ringing can manifest itself as systematic biases in some reconstructed spectral bands and can reduce the effectiveness of compression of spatially-low-pass subbands.

One of the two methods is denoted mean subtraction. The basic idea of this
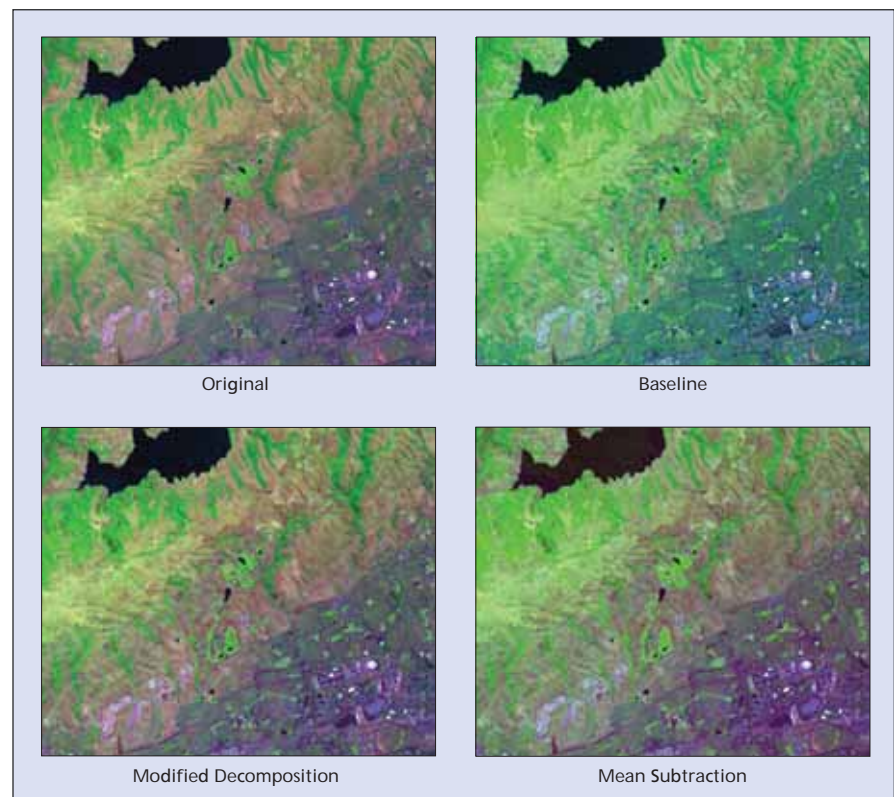


These false-color **Images of Terrain** at Moffett Field, California include an original image formed from three spectral bands and three different similarly-formed versions as reconstructed after 3D wavelet-based compression of the original image to 0.1 bits/sample.

method is to subtract mean values from spatial planes of spatially low-pass subbands prior to encoding, because (a) such spatial planes often have mean values that are far from zero and (b) zero-mean data are better suited for compression by methods that are effective for subbands of two-dimensional (2D) images. In this method, after the 3D wavelet decomposition is performed, mean values are computed for and subtracted from each spatial plane of each

spatially-low-pass subband. The resulting data are converted to sign-magnitude form and compressed in a manner similar to that of a baseline hyperspectral-image-compression method. The mean values are encoded in the compressed bit stream and added back to the data at the appropriate decompression step. The overhead incurred by encoding the mean values — only a few bits per spectral band — is negligible with respect to the huge size of a typical hyperspectral data set.

The other method is denoted modified decomposition. This method is so named because it involves a modified version of a commonly used multiresolution wavelet decomposition, known in the art as the 3D Mallat decomposition, in which (a) the first of multiple stages of a 3D wavelet transform is applied to the entire dataset and (b) subsequent stages are applied only to the horizontally-, vertically-, and spectrally-low-pass subband from the preceding stage. In the modified decomposition, in stages after the first, not only is the spatially-low-pass, spectrally-low-pass subband further decomposed, but also spatially-low-pass, spectrally-high-pass subbands are further decomposed spatially.

Either method can be used alone to improve the quality of a reconstructed image (see figure). Alternatively, the two methods can be combined by first performing modified decomposition, then subtracting the mean values from spatial planes of spatially-low-pass subbands.

*This work was done by Matthew Klimesh, Aaron Kiely, Hua Xie, and Nazeeh Aranki of Caltech for NASA's Jet Propulsion Laboratory. For further information, contact iaoffce@jpl.nasa.gov. NPO-41381*

# Improved Signal Chains for Readout of CMOS Imagers
## Two major imitations of prior readout signal chains are overcome.
*NASA's Jet Propulsion Laboratory, Pasadena, California*

An improved generic design has been devised for implementing signal chains involved in readout from complementary metal oxide/semiconductor (CMOS) image sensors and for other readout integrated circuits (ICs) that perform equivalent functions. The design applies to any such IC in which output signal charges from the pixels in a given row are transferred simultaneously into sampling capacitors at the bottoms of the columns, then voltages representing individual pixel charges are read out in sequence by sequentially turning on column-selecting field-effect transistors (FETs) in synchronism with source-follower- or operational-amplifier-based amplifier circuits.

The improved design affords the best features of prior source-follower-and operational-amplifier-based designs while overcoming the major limitations of those designs. The limitations can be summarized as follows:

• For a source-follower-based signal chain, the ohmic voltage drop associated with DC bias current flowing through the column-selection FET causes unacceptable voltage offset, non-linearity, and reduced small-signal gain.

• For an operational-amplifier-based signal chain, the required bias current and the output noise increase superlinearly with size of the pixel array because of a corresponding increase in the effective capacitance of the row bus used to couple the sampled column charges to the operational amplifier. The effect of the bus capacitance is to simultaneously slow down the readout circuit and increase noise through the Miller effect.

The improved design (see figure) provides a switched source follower in each column, one each for the signal and reference samples [denoted an in-column switched source follower ($ICS^2F$)], followed by a single capacitive transimpedance amplifier (CTIA) gain stage. The $ICS^2F$ consists of a different configuration of the column-selecting FET such that no DC bias current flows through it, and hence, without the associated ohmic voltage drop. Unlike in a prior operational-amplifier-based design involving direct connection of the sample and hold capacitors to the row-bus, the input terminals of the amplifier present CTIA gain stage are not in direct contact with the bus and, therefore, this stage produces voltage gain without the bandwidth reduction and noise multiplication that is caused by the Miller effect. Secondly, as a result of using $ICS^2Fs$, the bus carries a predominantly voltage signal, (as opposed to a predominantly
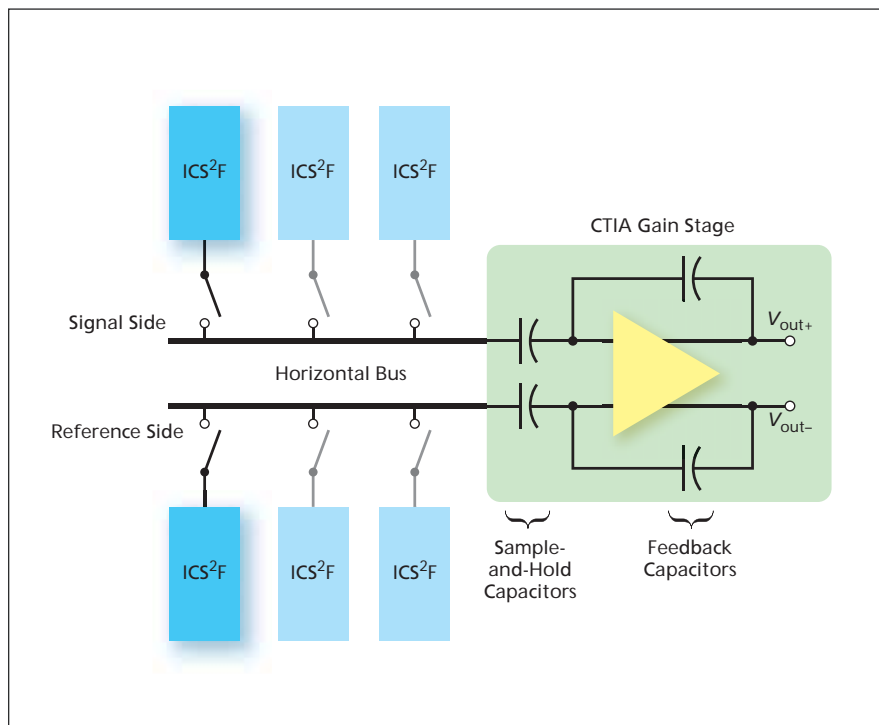


The **Improved Design** affords the best features of prior source-follower and operational-amplifier designs.

charge signal as in a prior operational-amplifier-based signal chain). Hence, the charging and discharging of the bus is not slowed by the Miller effect, enabling reduction of the bias current from the value that would otherwise be needed. The elimination of the ohmic drop across the column-selecting switch reduces the output voltage offset to a minimum, eliminates nonlinearity, and makes the small-signal gain approach its ideal value of unity.

*This work was done by Bedabrata Pain, Bruce Hancock, and Thomas Cunningham of Caltech for NASA's Jet Propulsion Laboratory.*

*In accordance with Public Law 96-517, the contractor has elected to retain title to this invention. Inquiries concerning rights for its commercial use should be addressed to:*

# SOI CMOS Imager With Suppression of Cross-Talk

## Potential applications are diverse, ranging from astronomy to medical imaging.

*NASA's Jet Propulsion Laboratory, Pasadena, California*

A monolithic silicon-on-insulator (SOI) complementary metal oxide/semiconductor (CMOS) image-detecting integrated circuit of the active-pixel-sensor type, now undergoing development, is designed to operate at visible and near-infrared wavelengths and to offer a combination of high quantum efficiency and low diffusion and capacitive cross-talk among pixels. The imager is designed to be especially suitable for astronomical and astrophysical applications. The imager design could also readily be adapted to general scientific, biological, medical, and spectroscopic applications.

One of the conditions needed to ensure both high quantum efficiency and low diffusion cross-talk is a relatively high reverse bias potential (between about 20 and about 50 V) on the photodiode in each pixel. Heretofore, a major obstacle to realization of this condition in a monolithic integrated circuit has been posed by the fact that the required high reverse bias on the photodiode is incompatible with metal oxide/semiconductor field-effect transistors (MOSFETs) in the CMOS pixel readout circuitry.

In the imager now being developed, the SOI structure is utilized to overcome this obstacle: The handle wafer is retained and the photodiode is formed in the handle wafer. The MOSFETs are formed on the SOI layer, which is separated from the handle wafer by a buried oxide layer. The electrical isolation provided by the buried oxide layer makes it possible to bias the MOSFETs at CMOS-compatible potentials (between 0 and 3 V), while biasing the photodiode at the required higher potential, and enables independent optimization of the sensory and readout portions of the imager.
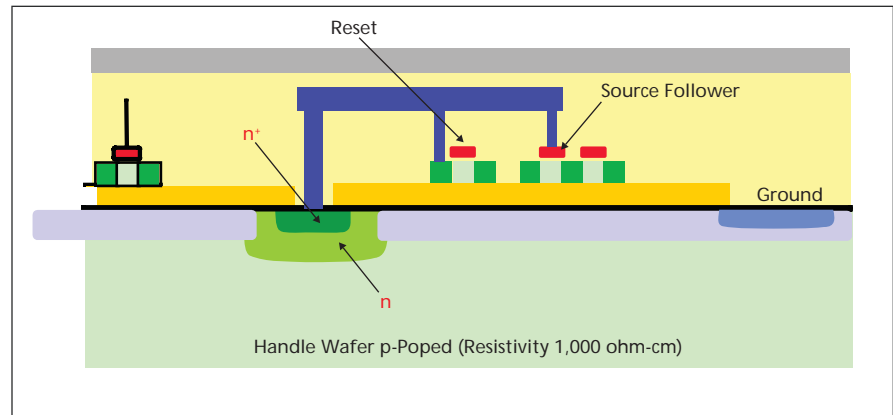


A **Photodiode Is Formed in the Handle Wafer** between an implanted n-doped well and the rest of the handle wafer, which is p-doped. This arrangement makes it possible to apply a high reverse bias to the diode, as needed for high quantum efficiency and low diffusion cross-talk.

The figure presents a simplified and partly schematic cross section of one pixel. The photodiode is formed, in the handle wafer, between an implanted deep n-doped well and the rest of the handle wafer. An $n^+$-doped cathode contact region in the well is electrically connected by a tungsten via plug to the source of a reset FET residing on the SOI layer. The bottom of the handle wafer is reverse-biased to 30 V, while the $n^+$-doped cathode contact region is subject to potential excursions of 1 to 2 V, which are within permissible voltage limits. The reverse bias of the handle wafer is brought in from the front side (the top side in the figure) through a $p^+$-doped anode guard ring positioned and dimensioned to prevent breakdown of Si or $SiO_2$ in the presence of the bias potential. An implanted boron pinning layer, biased at a small negative potential, holds the interface between the buried oxide and the handle-wafer silicon in equilibrium and thereby helps to minimize dark current.

The potential difference ($\oplus$30 V) between the pinning layer and the bottom of the handle wafer could result in undesired ohmic conduction between them. Therefore, the doping profiles are chosen in conjunction with the device geometry (including the dimensions of, and spacing between, the n-doped wells) to shape the electric field to create a pinch-off region (a potential barrier) that prevents such conduction. The pinch-off region also prevents electric-field coupling between adjacent n-doped wells, thereby eliminating inter-pixel capacitance and the associated capacitive cross-talk between pixels.

The reset FET is, more specifically, an n-type FET, chosen to prevent inadvertent forward-biasing of the sensory node during reset-switch turn-off. The back and front gates of the reset FET are connected to each other in order to set the minimum anode potential such that the pinch-off condition is maintained for all illumination conditions.

This configuration also increases the reverse bias of the reset FET, preventing parasitic conduction in the FET channel, thereby suppressing sensory-node leakage.

*This work was done by Bedabrata Pain, Xinyu Zheng, Thomas J. Cunningham, Suresh Seshadri, and Chao Sun of Caltech for NASA's Jet Propulsion Laboratory. Further information is contained in a TSP (see page 1).*

*In accordance with Public Law 96-517, the contractor has elected to retain title to this invention. Inquiries concerning rights for its commercial use should be addressed to:*

# Error-Rate Bounds for Coded PPM on a Poisson Channel

## It is now possible to calculate tight bounds at high SNR.

*NASA's Jet Propulsion Laboratory, Pasadena, California*

Equations for computing tight bounds on error rates for coded pulse-position modulation (PPM) on a Poisson channel at high signal-to-noise ratio have been derived. These equations and elements of the underlying theory are expected to be especially useful in designing codes for PPM optical communication systems.

The equations and the underlying theory apply, more specifically, to a case in which

- At the transmitter, a linear outer code is concatenated with an inner code that includes an accumulator and a bit-to-PPM-symbol mapping (see figure) [this concatenation is known in the art as "accumulate-PPM" (abbreviated "APPM")];
- The transmitted signal propagates on a memoryless binary-input Poisson channel; and
- At the receiver, near-maximum-likelihood (ML) decoding is effected through an iterative process.

Such a coding/modulation/decoding scheme is a variation on the concept of turbo codes, which have complex structures, such that an exact analytical expression for the performance of a particular code is intractable. However, techniques for accurately estimating the performances of turbo codes have been developed. The performance of a typical turbo code includes (1) a "waterfall" region consisting of a steep decrease of
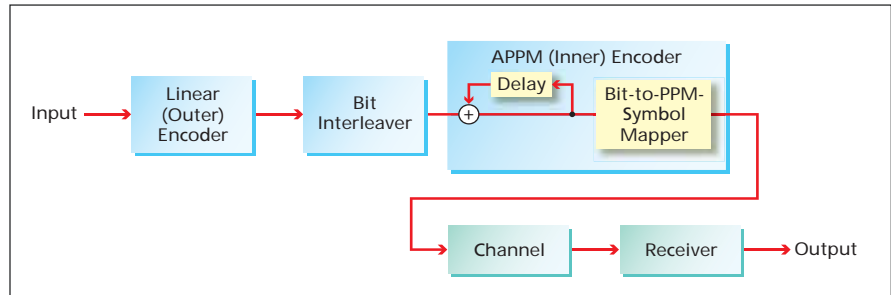


**Two Codes Are Concatenated** in a PPM system of the type to which the present innovations apply.

error rate with increasing signal-to-noise ratio (SNR) at low to moderate SNR, and (2) an "error floor" region with a less steep decrease of error rate with increasing SNR at moderate to high SNR.

The techniques used heretofore for estimating performance in the waterfall region have differed from those used for estimating performance in the error-floor region. For coded PPM, prior to the present derivations, equations for accurate prediction of the performance of coded PPM at high SNR did not exist, so that it was necessary to resort to time-consuming simulations in order to make such predictions. The present derivation makes it unnecessary to perform such time-consuming simulations.

Because a mathematically complete description of the derivation and equations would greatly exceed the space available for this article, it must suffice

to summarize the three most novel aspects:

- For purposes of analysis, *M*-ary PPM was treated as equivalent to a binary code of rate $\log_2(M)/M$ (where *M* is an integer >1). This treatment was necessary for modeling of the iterative demodulation/decoding process.
- Closed-form expressions for input-output-weight-enumerator functions for PPM and APPM were derived for the first time.
- An improvement to the union bound for a Poisson channel was derived and shown to be extensible to low SNR.
- The union bound was shown to be applicable for PPM, a nonlinear code.

*This work was done by Bruce Moision and Jon Hamkins of Caltech for NASA's Jet Propulsion Laboratory. For further information, contact iaoffice@jpl.nasa.gov. NPO-42990*

# Biomorphic Multi-Agent Architecture for Persistent Computing

## Computing systems would reconfigure themselves to continue functioning despite failures of components.

*Langley Research Center, Hampton, Virginia*

A multi-agent software/hardware architecture, inspired by the multicellular nature of living organisms, has been proposed as the basis of design of a robust, reliable, persistent computing system. Just as a multicellular organism can adapt to changing environmental conditions and can survive despite the failure of individ-

ual cells, a multi-agent computing system, as envisioned, could adapt to changing hardware, software, and environmental conditions. In particular, the computing system could continue to function (perhaps at a reduced but still reasonable level of performance) if one or more component(s) of the system were to fail.

One of the defining characteristics of a multicellular organism is unity of purpose. In biology, the purpose is survival of the organism. The purpose of the proposed multi-agent architecture is to provide a persistent computing environment in harsh conditions in which repair is difficult or impossible.

FAILURE OF MIDDLE SENSOR CELL

SUBSTITUTION OF BOTTOM SENSOR CELL FOR FAILED MIDDLE SENSOR CELL
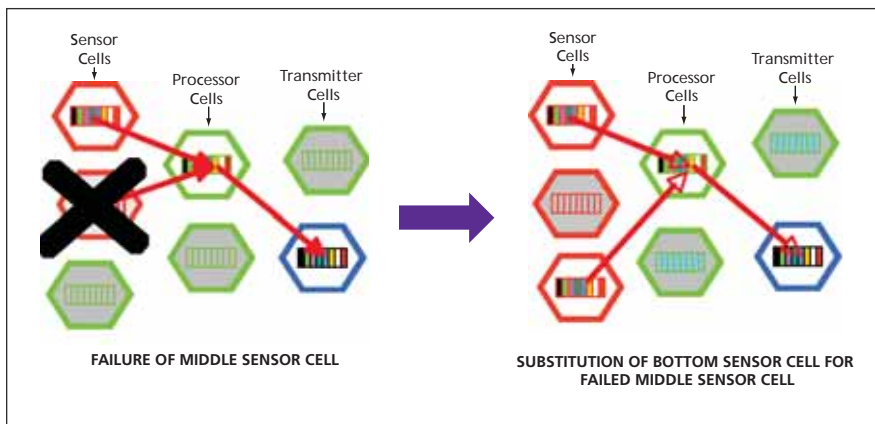
This **Simulated Prototype System** contained three sensor cells (the lowest one of which one was initially a spare), two general-purpose processor cells, and two radio-transmitter cells. Failure of the middle sensor cell initiated a biomorphic process that placed the spare sensor cell into service.

A multi-agent, organismlike computing system would be a single entity built from agents or cells. Each agent or cell would be a discrete hardware processing unit that would include a data processor with local memory, an internal clock, and a suite of communication equipment capable of both local line-of-sight communications and global broadcast communications. Some cells, denoted specialist cells, could contain such additional hardware as sensors and emitters. Each cell would be independent in the sense that there would be no global clock, no global (shared) memory, no pre-assigned cell identifiers, no pre-defined network topology, and no centralized brain or control structure. Like each cell in a living organism, each agent or cell of the computing system would contain a full description of the system encoded as genes, but in this case, the genes would be components of a software genome.

Although the cells would be independent in the sense described above, they would be tightly coupled and logically interdependent in that they would exchange information and respond accordingly. The software genome would program the system at two distinct levels: The first-level programs would describe the intercellular flow of data and control information. The second level programs would consist of program fragments conceptually similar to traditional software library modules. Each agent or cell would choose which gene to express, depending on the internal state of the cell, the genome, and the states of neighboring cells. Gene expression in each cell would involve executing a program fragment, which, when combined with all other genes in the genome, would define the full system. Because the mapping of program fragments to particular cells would not be explicitly defined, the program could run on an arbitrary configuration of cells. Indeed, cells could be added to the system (hardware upgrade) or removed (hardware failure) during operation, and the system would reconfigure itself to utilize the currently operational hardware without losing functionality. This capability for self configuration, among other capabilities, was demonstrated in a software simulation of a prototype seven-cell system (see figure).

*This work was done by Kenneth N. Lodding and Paul Brewster of Langley Research Center. Further information is contained in a TSP (see page 1).*
*LAR-16857-1*

# Using Covariance Analysis To Assess Pointing Performance

*NASA's Jet Propulsion Laboratory, Pasadena, California*

A Pointing Covariance Analysis Tool (PCAT) has been developed for evaluating the expected performance of the pointing control system for NASA's Space Interferometry Mission (SIM). The SIM pointing control system is very complex, consisting of multiple feedback and feedforward loops, and operating with multiple latencies and data rates. The SIM pointing problem is particularly challenging due to the effects of thermomechanical drifts in concert with the long camera exposures needed to image dim stars.

Other pointing error sources include sensor noises, mechanical vibrations, and errors in the feedforward signals. PCAT models the effects of finite camera exposures and all other error sources using linear system elements. This allows the pointing analysis to be performed using linear covariance analysis. PCAT propagates the error covariance using a Lyapunov equation associated with time-varying discrete and continuous-time system matrices. Unlike Monte Carlo analysis, which could involve thousands of computational runs for a single assessment, the PCAT analysis performs the same assessment in a single run. This capability facilitates the analysis of parametric studies, design trades, and "what-if" scenarios for quickly evaluating and optimizing the control system architecture and design.

*This work was done by David Bayard and Bryan Kang of Caltech for NASA's Jet Propulsion Laboratory. Further information is contained in a TSP (see page 1).*
*3NPO-45308*

National Aeronautics and
Space Administration